White Rose Research Online

eprints@whiterose.ac.uk
https://eprints.whiterose.ac.uk
Universities of Leeds, Sheffield and York

Deposited via The University of York.

White Rose Research Online URL for this paper:
https://eprints.whiterose.ac.uk/id/eprint/247203/

Version: Published Version

Article:
Jeanquartier, Fabien, Graves, Jonathan P., Brunner, Stephan et al. (2026) Study of kinetic effects on MHD instabilities in cylindrical geometry using a spectral hybrid kinetic-MHD code. Plasma Physics and Controlled Fusion. 075020. ISSN: 1361-6587

https://doi.org/10.1088/1361-6587/ae7c30

Reuse
This article is distributed under the terms of the Creative Commons Attribution (CC BY) licence. This licence allows you to distribute, remix, tweak, and build upon the work, even commercially, as long as you credit the authors for the original work. More information and the full terms of the licence here:
https://creativecommons.org/licenses/

Takedown
If you consider content in White Rose Research Online to be in breach of UK law, please notify us by emailing eprints@whiterose.ac.uk including the URL of the record and the reason for the withdrawal request.

UNIVERSITY OF LEEDS
University of Sheffield
UNIVERSITY of York

Plasma Physics and
Controlled Fusion

PURPOSE-LED
PUBLISHING™

PAPER • **OPEN ACCESS**

Study of kinetic effects on MHD instabilities in cylindrical geometry using a spectral hybrid kinetic-MHD code

To cite this article: Fabien Jeanquartier *et al* 2026 *Plasma Phys. Control. Fusion* **68** 075020

View the article online for updates and enhancements.

You may also like

- Turbulent Equilibria for Charged Particles in Space
Peter H. Yoon
- Fundamental Physical Parameter Fitting via Electrochemical Impedance Spectroscopy
Fazl Eren Civan, Gökberk Katrc and Burak Ülgüt
- Impact of time-of-flight on indirect 3D and direct 4D parametric image reconstruction in the presence of inconsistent dynamic PET data
F A Kotasidis, A Mehranian and H Zaidi

This content was downloaded from IP address 144.32.240.131 on 26/10/2026 at 11:56

Plasma Physics and Controlled Fusion

Check for updates

OPEN ACCESS

RECEIVED
20 February 2026

REVISED
28 May 2026

ACCEPTED FOR PUBLICATION
11 June 2026

PUBLISHED
14 July 2026

Original content from this work may be used under the terms of the Creative Commons Attribution 4.0 licence.

Any further distribution of this work must maintain attribution to the author(s) and the title of the work, journal citation and DOI.

PAPER

Study of kinetic effects on MHD instabilities in cylindrical geometry using a spectral hybrid kinetic-MHD code

Fabien Jeanquartier[1,*], Jonathan P Graves[1,2], Stephan Brunner[1], Guillermo Bustos Ramirez[3], Tom Emerit[4], Samuel Lanthaler[1] and Amélie Renggli[1]

[1] École Polytechnique Fédérale de Lausanne (EPFL), Swiss Plasma Center (SPC), CH-1015 Lausanne, Switzerland
[2] Department of Physics, York Plasma Institute, University of York, York, Heslington YO10 5DD, United Kingdom
[3] Department of Applied Physics and Applied Mathematics, Columbia University, New York, NY 10027, United States of America
[4] CNRS, PIIM, Aix Marseille Univ, Marseille, France
[*] Author to whom any correspondence should be addressed.

E-mail: fabien.jeanquartier@epfl.ch

Keywords: kinetic-MHD, fusion, instabilities, Case–Van Kampen approach

Abstract

Machine-scale instabilities in fusion devices are commonly described using magnetohydrodynamics (MHD), however kinetic effects can significantly affect MHD instabilities through kinetic compression and wave-particle interaction. We propose a new code that solves the drift-kinetic-MHD equations using a spectral method, formulated using a Case–Van Kampen approach (Van Kampen (1955 *Physica* **21** 949)). The eigenvectors of the standardised eigenvalue problem are composed of the perpendicular MHD-like displacement, a potential that describes the parallel electric field, as well as the kinetic correction to the perturbed distribution function. The new code, which can solve for generalised kinetic equilibria in axisymmetric toroidal geometry, is benchmarked favourably against exact analytic solutions for kinetic-MHD in a cylindrical screw pinch. In this configuration, kinetic effects are driven by the particles in the long free path limit subject to angular drifts associated with the radial curvature of the configuration. The kinetic effect of highly energetic particles is shown to be stabilising via exact cancellation of ideal MHD interchange (Suydam), while for moderately energetic particles, their effective guiding centre velocity resonates with the wave frequency, causing novel kinetic instabilities in the cylinder.

1. Introduction

Large scale plasma instabilities in tokamaks are well described by fluid models such as ideal magnetohydrodynamics (MHD). Most of these instabilities must be avoided when operating the device, as they can disrupt the plasma or even damage the machine. Tokamaks contain energetic particles, such as fusion products or auxiliary heated particles, that cannot be fully described by fluid theory. Kinetic corrections alter the growth rate and stability thresholds of large scale instabilities. A suitable solution for addressing these issues is that of so-called kinetic-MHD models, which treat kinetic effects as a correction to the fundamentally ideal MHD model. One way to take into account kinetic effects is to insert kinetically computed pressures in the MHD momentum equation. The kinetic pressures are obtained by computing moments of a distribution function that evolves in time according to a Vlasov-type equation (Park *et al* 1992). The drift-kinetic equation serves as closure for the model, thus replacing the adiabatic equation of state for the ideal MHD model. A linear study is justified by its cheap computational cost and its relevant predictions for the onset of linear instabilities that are precursors of non-linear instabilities observed in practice. Several existing works already implemented this idea. Such problems can be solved either using an explicit time evolution approach for the kinetic part or a spectral approach. The first option is followed by codes such `XTOR-K` (Lütjens and Luciani 2010), `ORB5` (Lanti *et al* 2020), `M3D-K` (Fu *et al* 2006), `HMGC` (Briguglio *et al* 1995, 1998) or `GTC` (Deng *et al* 2012), which time evolve the full trajectories

© 2026 The Author(s). Published by IOP Publishing Ltd

and use a particle-in-cells approach. For a more complete overview, see for example Vlad *et al* (2025). The time evolution approach is however very expensive numerically, especially in cases such as the one considered here where the spectrum aspect ratio (see definition later) is very large, which constrains the possible time-steps to very small values.

An alternative option is to use a spectral approach. It is possible with this method to obtain sub-dominant modes, unlike the time evolution approach, which can only find the most unstable mode. The drawback is that it cannot be generalised to a non-linear case. Two main options exist for solving the spectral kinetic-MHD problem. The first, *Landau approach*, consists in solving the drift-kinetic equation analytically and inserting the result in the MHD momentum equation, yielding a non-linear eigenvalue problem for the MHD displacement and the frequency. Careful integration of the resonant denominators appearing in the perturbed pressures is required. This is often done partially analytically under some assumptions. Codes such as `MARS-K` (Liu *et al* 2009), `NOVA-K` (Cheng 1992) or `LIGKA` (Lauber *et al* 2007) are based on this approach.

The approach followed in this work is to keep the system of equations formed by the MHD momentum equation along with the drift-kinetic equation and express it as a standard linear eigenvalue problem for the MHD variables and the perturbed distribution function as well as the mode frequency. The resulting problem is much larger but is linear in the eigenvalue ω, and it does not have intrinsic poles to handle over phase space integration. This *Case–Van Kampen approach* is also straightforwardly generalisable to non-linear cases. The spectral version of the gyrokinetic code `GENE` (Jenko *et al* 2000) follows this approach. In this work, we propose solving the kinetic-MHD equations as an eigenvalue problem using a new spectral code, `VENUS-KMHD`, based on the existing ideal MHD code `VENUS-MHD` (Bustos Ramirez 2023, Schaumans and Graves 2025). Following the Case–Van Kampen approach, we solve simultaneously both sets of equations, which means the eigenvector now consists in the MHD variables and the kinetic variables. This has the significant advantage that the obtained eigenvalue problem is standard, in the sense that it is linear in the eigenvalue ω, such that existing libraries can be used to solve the discretised problem. Unlike kinetic-MHD codes using the Landau approach, the implementation is straightforward even without approximation on the particle orbits. Moreover, a drift-kinetic equation is used to describe the evolution of the kinetic distribution function, which avoids problems linked to the validity domain of the gyrokinetic approximation that arise when describing large scale MHD modes, in particular current-driven modes (McMillan 2023). In this paper, we will investigate instabilities in cylindrical geometry, which corresponds to a straightened tokamak with no toroidal effects, a so-called screw pinch. Using a Fourier representation for the poloidal and toroidal directions, cylindrical cases require significantly less numerical resources than toroidal cases of comparable radial and velocity space resolutions thanks to the lack of poloidal modes coupling. This reduced numerical cost is very useful to do preliminary tests of a new code. Moreover, it is possible in cylindrical geometry to obtain exact analytical results for several relevant quantities which can then be used to benchmark the code. Because the considered matrices are very large but very sparse, it is crucial to use an appropriate method to solve the eigenvalue problem. The mode of physical interest, which are usually the most unstable ones, cannot be obtained using a simple power method to iteratively solve the eigenvalue problem. The spectrum of the problem presents a very high aspect ratio. It is strongly elongated along the imaginary axis, corresponding to the convective dynamics, but weakly elongated along the real axis, corresponding to unstable and damped dynamics. As a consequence, the most unstable modes, despite being at the periphery of the spectrum, are subdominant in the sense that their magnitude is much smaller than the fastest convective stable modes. As a result, particular care is necessary in order to be able to find the modes of interest efficiently and correctly, without requesting unrealistic amounts of computational resources. Note however, that like `VENUS-MHD`, the new `VENUS-KMHD` code is already capable of solving toroidal cases, based on profiles obtained with an equilibrium code such as `VMEC` (Hirshman and Whitson 1983). Kinetic-MHD results in tokamak geometry will be presented in a future publication. Toroidal results obtained with the ideal version `VENUS-MHD` are presented in Bustos Ramirez (2023), Schaumans and Graves (2025). The remainder of this paper is organised as follows: in section 2, the kinetic-MHD model we use is introduced, first in the general case and then in the specific case of cylindrical geometry with a single kinetic species, which is the main focus of this work. The `VENUS-KMHD` code used for this work is briefly described in section 3. A more detailed description of the numerical approach will be presented in a future dedicated publication. Section 4 presents the different benchmarks that were undertaken in cylindrical geometry, first for the kinetic perturbed distribution function, then for the associated kinetic perturbed pressures. Benchmarking of the complete kinetic-MHD problem is then demonstrated in the very low and very large frequency limits. Physical conclusions are presented for the novel stabilising kinetic effects uncovered. Finally, a few full physical cases are studied in section 5, still in cylindrical geometry, to test the general possibilities of the code. In particular, it is shown that kinetic instabilities exist by

virtue of the radial curvature of the cylinder and resonance between wave and guiding centre motion of energetic ions.

2. Kinetic-MHD model

2.1. Presentation of the general model

We start this section considering the general case of an axisymmetric system (tokamak geometry), specialising in the cylindrical limit later on. We aim at a linear description of the kinetic-MHD problem. The equations are linearised around an equilibrium configuration, which is either given by an analytical result or obtained with an equilibrium code. The model proposed by Lanthaler *et al* (2019), Lanthaler (2020) is used. Note that many papers have been written on kinetic-MHD instabilities (many are cited in Lanthaler *et al* (2019)), including by the co-authors of this paper, but Lanthaler (2020) develops a novel rigorous derivation for finite Larmor radius corrections (inertial diamagnetic effects) for populations in the long mean free path, and has shown that the drift-kinetic model is accurate to higher order in Larmor radius than was previously appreciated. The advantages of kinetic-MHD over standard gyrokinetic closure deployed turbulence codes was clarified.

The kinetic-MHD model consists mainly of the MHD momentum conservation equation as well as a drift-kinetic equation for each species which is treated kinetically. The kinetic effects enter into the MHD momentum equation through corrections to the perturbed pressure. The perturbed electromagnetic fields couple the drift-kinetic equations to the MHD momentum equation and are expressed in terms of the MHD variables. A quasi-neutrality equation is used to close the system. Because our main focus is long wavelength modes, certain finite Larmor radius effects can be neglected for the kinetic species and we therefore use a drift-kinetic equation, instead of a gyrokinetic equation.

In this work, we consider cases with no equilibrium flows. They are not taken into account both in the equilibrium configuration and in the stability computation. The model we use from Lanthaler *et al* (2019), Lanthaler (2020) considers the effect of strong flows, including centrifugal effects, but the corresponding terms are removed here. It is known that even weak sheared flows can have an impact on kinetic effects (Graves *et al* 2000). These effects are nevertheless not considered here. The inclusion of weak sheared flows and then strong flows will be the object of future work.

At first, the most general model, including all effects included in Lanthaler *et al* (2019), Lanthaler (2020) (except equilibrium flows) is presented. In this first part, all the species are considered to be simulated kinetically. The case where only some of the species are kinetic will be considered at the end of this section. In the kinetic description, each species k is represented by a distribution function f_k which is decomposed into a background distribution F_k, chosen in advance and kept fixed throughout the simulation and fluctuations, which can in turn be decomposed into two types: adiabatic and non-adiabatic,

$$f_k = F_k + \delta f_k = F_k + \delta f_{\mathrm{adiab}_k} + \delta h_k. \tag{1}$$

Note that a list of symbols used in this work is provided in appendix A. The evolution of δh_k is dictated by an effective drift-kinetic equation. The considered dependent variables are $\boldsymbol{\xi}$ (the MHD displacement) and $\delta\phi$ (the perturbed electrostatic potential) for the MHD part as well as δh_k (non-adiabatic fluctuation of the distribution function of kinetic species k) for the kinetic part.

The magnetic field fluctuations $\boldsymbol{\delta B}$ are expressed in terms of the fluctuating vector potential $\boldsymbol{\delta A}$, $\boldsymbol{\delta B} = \boldsymbol{\nabla} \times \boldsymbol{\delta A}$. We consider the gauge $\boldsymbol{\delta A} \cdot \boldsymbol{b} = \delta A_{\parallel} = 0$ (the component of $\boldsymbol{\delta A}$ parallel to the equilibrium magnetic field is zero), with $\boldsymbol{b} = \boldsymbol{B}/||\boldsymbol{B}|| = \boldsymbol{B}/B$ ($\boldsymbol{B}$ stands for the equilibrium magnetic field). As a result, the perturbed fields are expressed as:

$$\boldsymbol{\delta A} = \boldsymbol{\xi} \times \boldsymbol{B}, \quad \boldsymbol{\delta E} = -\frac{\partial}{\partial t}(\boldsymbol{\delta A}) - \boldsymbol{\nabla}\delta\phi, \quad \boldsymbol{\delta B} = \boldsymbol{\nabla} \times \boldsymbol{\delta A}. \tag{2}$$

Note that this gauge choice implies that the component $\delta E_{\parallel} = \boldsymbol{\delta E} \cdot \boldsymbol{b}$ of the perturbed electric field $\boldsymbol{\delta E}$ parallel to the equilibrium magnetic field is entirely determined by the scalar potential $\delta\phi$, since $\boldsymbol{\delta A}$ is perpendicular to $\boldsymbol{B}$ and has therefore no parallel component.

Because we are not considering equilibrium flows, the equilibrium quantities satisfy the simple force balance equation:

$$\boldsymbol{j} \times \boldsymbol{B} = \frac{1}{\mu_0}(\boldsymbol{\nabla} \times \boldsymbol{B}) \times \boldsymbol{B} = \boldsymbol{\nabla} P, \tag{3}$$

where P is the total pressure, $P = \sum_k P_k$. The axisymmetric and divergence free equilibrium magnetic field is written as follows in the general case:

$$\boldsymbol{B} = F\boldsymbol{\nabla}\varphi + \boldsymbol{\nabla}\varphi \times \boldsymbol{\nabla}\psi, \tag{4}$$

where φ is the toroidal angle, F is the flux function[5] and ψ is the poloidal magnetic flux, $\psi = -\frac{1}{2\pi}\int \boldsymbol{B}\cdot \mathrm{d}\boldsymbol{S_p}$ with $\mathrm{d}\boldsymbol{S_p}$ oriented in the direction of the poloidal angle θ close to the vertical axis of the torus. The focus of this study is on modes of long wavelength and of frequency much lower than the cyclotron frequency. The drift-kinetic description for the kinetic species is therefore appropriate. A two-dimensional velocity space representation is sufficient as the gyroangle is averaged out and does not appear in the equations. We use $v_\parallel$, the parallel velocity, and $\mu = \frac{m_k v_\perp^2}{2B}$, the magnetic moment, as the two explicit velocity variables. This choice is inspired by gyrokinetic codes such as GENE (Jenko *et al* 2000). One drawback compared to some popular choices for analytical work such as $(\mathcal{E}, \mu, \sigma = \mathrm{sign}(v_\parallel))$ or $(\mathcal{E}, \lambda, \sigma)$ ($\lambda = \mu/\mathcal{E}$ is the pitch angle) is that unlike $\mathcal{E}, \mu$ and λ, $v_\parallel$ is not a constant of motion. The main advantage for the numerical resolution is that the sign σ of the parallel velocity is explicitly known and it is not necessary to handle an extra variable for this purpose. One can note that in a cylinder, σ is a constant of motion. In a torus however, this would be the case only for passing particles while trapped particles trajectories cover both signs of σ. Moreover, the sign change occurs at locations that are hard to determine in advance.

The linearised MHD momentum equation is modified in a fundamental way by kinetic corrections. With the effect of the perturbed electrostatic potential but without equilibrium flows, one has (Antonsen and Bondeson (1993), Graves and Wahlberg (2017), Lanthaler *et al* (2019), Lanthaler (2020)):

$$\begin{aligned}\sum_k \rho_k \left[\left(\frac{\partial}{\partial t} + \boldsymbol{u}_{*_k}\cdot\boldsymbol{\nabla}\right)\frac{\partial \boldsymbol{\xi}_\perp}{\partial t} - \left(\frac{\partial}{\partial t} + \boldsymbol{u}_{*_k}\cdot\boldsymbol{\nabla}\right)\left(\frac{\boldsymbol{\nabla}\delta\phi \times \boldsymbol{B}}{B^2}\right)\right] \\ = \boldsymbol{\delta j}\times\boldsymbol{B} + \boldsymbol{j}\times\boldsymbol{\delta B} + \boldsymbol{b}\frac{\mathrm{d}P}{\mathrm{d}r}(\boldsymbol{b}\cdot\boldsymbol{\nabla}\xi_\perp^r) + \sum_k \left[\left(\delta P_{\perp_k}^{\mathrm{tot}} - \delta P_{\parallel_k}^{\mathrm{tot}}\right)\boldsymbol{\kappa} - \boldsymbol{\nabla}_\perp \delta P_{\perp_k}^{\mathrm{tot}}\right].\end{aligned} \tag{5}$$

Note that this expression is obtained by projecting the momentum equation with the perpendicular component of the full magnetic field $\boldsymbol{B} + \boldsymbol{\delta B}$, while the definition of $\perp$ in equation (5) remains that the quantity it is assigned to is perpendicular to the equilibrium $\mathbf{B}$. In particular, the third term in the second line of equation (5) results from the projection perpendicular to the total magnetic field of the pressure gradient term and is given by $\boldsymbol{b}(\boldsymbol{\delta b}\cdot\boldsymbol{\nabla})P_k \simeq \boldsymbol{b}(\mathrm{d}P_k/\mathrm{d}r)(\boldsymbol{b}\cdot\boldsymbol{\nabla}\xi_\perp^r)$, with $\boldsymbol{\delta b} = \boldsymbol{\delta B}/|\boldsymbol{\delta B}|$. Note that this is exact in a cylinder and a very good approximation in the torus. This corresponds to the terms in blue in equation (14) of Zhang *et al* (2024) in the limit of isotropic equilibrium. Here, $\rho_k = m_k n_k$ is the mass density of species k with m_k the mass and n_k the number density of the species, $\boldsymbol{u}_{*_k} = \frac{1}{q_k B n_k}\boldsymbol{b}\times\boldsymbol{\nabla}P_k$ is the diamagnetic flow velocity for species k, $\boldsymbol{\xi}_\perp = \boldsymbol{\xi} - (\boldsymbol{\xi}\cdot\boldsymbol{b})\boldsymbol{b}$ is related to the perpendicular fluid displacement (see later, it has two independent components $\xi_\perp^r$ and $\xi_\perp^\perp$), $\delta P_{\perp_k}^{\mathrm{tot}}, \delta P_{\parallel_k}^{\mathrm{tot}}$ are the perpendicular and parallel perturbed pressures for kinetic species k and $\boldsymbol{\kappa} = (\boldsymbol{b}\cdot\boldsymbol{\nabla})\boldsymbol{b}$ is the magnetic field line curvature.

The perturbed pressures are given by corresponding moments of the perturbed distribution function:

$$\delta P_{\perp_k}^{\mathrm{tot}} = 2\pi\int_{-\infty}^{\infty}\mathrm{d}v_\parallel\int_0^\infty \mathrm{d}\mu\,\mu\frac{B^2}{m_k}\delta f_k, \quad \delta P_{\parallel_k}^{\mathrm{tot}} = 2\pi\int_{-\infty}^{\infty}\mathrm{d}v_\parallel\int_0^\infty \mathrm{d}\mu\, v_\parallel^2 B\delta f_k, \tag{6}$$

where the *tot* superscript indicates that these perturbed pressures are computed from the full δf_k, which means they include the adiabatic perturbations due to $\delta f_{\mathrm{adiab}_k}$ and the kinetic perturbations due to δh_k (see equation (1)). In our case, the perturbed distribution can be written explicitly as (Lanthaler (2020)):

$$\delta f_k = q_k R^2(\boldsymbol{\xi}_\perp\times\boldsymbol{B})\cdot\boldsymbol{\nabla}\varphi\frac{\partial F_k}{\partial P_\varphi} + q_k\delta\phi\frac{\partial F_k}{\partial\mathcal{E}} - \mu\frac{\delta B_\parallel}{B}\frac{\partial F_k}{\partial\mu} + \delta h_k. \tag{7}$$

The evolution of the non-adiabatic component δh_k of the perturbed distribution function of kinetic species k is described by the following effective linearised drift-kinetic equation (Porcelli *et al* 1994,

[5] Note that to prevent confusion between F appearing in equation (3) and the equilibrium distribution F_k of species k (see equation (1)), the latter always has the index of the species to which it belongs.

Lanthaler 2020):

$$\left(\frac{\partial}{\partial t}-\frac{1}{m_k}\left(\mu\boldsymbol{b}\cdot\boldsymbol{\nabla}B-m_k v_{\parallel}\boldsymbol{\kappa}\cdot\boldsymbol{v}_{g_k}\right)\frac{\partial}{\partial v_{\parallel}}+\boldsymbol{v}_{g_k}\cdot\boldsymbol{\nabla}\right)\delta h_k = \left(\frac{\partial F_k}{\partial\mathcal{E}}\frac{\partial}{\partial t}-\frac{\partial F_k}{\partial P_\varphi}\frac{\partial}{\partial\varphi}\right)\left(q_k\left(\boldsymbol{\xi}_\perp\times\boldsymbol{B}\right)\cdot\boldsymbol{v}_{g_k}-q_k\delta\phi-\mu\delta B_{\parallel}\right), \tag{8}$$

where $\mathcal{E}=m_k v_{\parallel}^2/2+m_k v_{\perp}^2/2=m_k v_{\parallel}^2/2+\mu B$ is the kinetic energy, m_k is the mass of kinetic species k, $\delta B_{\parallel}=\boldsymbol{\delta B}\cdot\boldsymbol{b}=(\boldsymbol{\nabla}\times(\boldsymbol{\xi}\times\boldsymbol{B}))\cdot\boldsymbol{b}$, q_k is the electric charge of kinetic species k and P_φ is the canonical momentum associated with φ. Note that since the velocity space coordinates are $(v_{\parallel},\mu)$ and because $v_{\parallel}$ is not a constant of motion, a term involving $\partial/\partial v_{\parallel}$ appears in the full time derivative of δh_k in (8). In equations (7) and (8), we have $F_k=F_k(\mathcal{E},P_\varphi,\mu)$, the constants of motion of the unperturbed system. The derivatives in $\mathcal{E},P_\varphi,\mu$ are evaluated with the other two variables kept constant. As a consequence, the $\partial F_k/\partial\mu$ term in (7) is zero for an isotropic equilibrium distribution function, as considered here. $\boldsymbol{v}_{g_k}$ is the guiding-centre velocity for species k and is defined as:

$$\boldsymbol{v}_{g_k}=v_{\parallel}\boldsymbol{b}+\boldsymbol{v}_{d_k}=v_{\parallel}\boldsymbol{b}+\boldsymbol{b}\times\left(\frac{1}{q_k B}\left(\mu\boldsymbol{\nabla}B+m_k v_{\parallel}^2\boldsymbol{\kappa}\right)\right). \tag{9}$$

The system is closed by the quasi-neutrality equation, where once again the perturbed mass density for each species is computed from the perturbed distribution function δf_k given by equation (7):

$$\sum_k q_k\int_{-\infty}^{\infty}\mathrm{d}v_{\parallel}\int_0^{\infty}\mathrm{d}\mu\delta f_k=0. \tag{10}$$

The spatial coordinates we use are straight-field line coordinates with r denoting the radial direction, θ the straight-field line poloidal direction and φ the toroidal direction. We express the dependence of the fluctuating quantities $\boldsymbol{\xi}_\perp,\delta\phi,\delta h_k$ in the toroidal and poloidal directions using a Fourier expansion with associated poloidal mode number m and toroidal mode number n. In a tokamak geometry, because of axisymmetry of the equilibrium, eigenmodes have an exact toroidal mode number while they couple in the toroidal direction and are therefore composed of several poloidal modes m. A Fourier mode representation is also used for the time dependence of all fluctuating quantities with associated complex frequency ω. The space and velocity dependence of our variables therefore read:

$$\boldsymbol{\xi}_\perp(\boldsymbol{x})=\sum_m\left(\boldsymbol{\xi}_\perp\right)_m(r)\,e^{i(m\theta+n\varphi-\omega t)}, \tag{11}$$

$$\delta\phi(\boldsymbol{x})=\sum_m\left(\delta\phi\right)_m(r)\,e^{i(m\theta+n\varphi-\omega t)}, \tag{12}$$

$$\delta h_k(\boldsymbol{x},\boldsymbol{v})=\sum_m\left(\delta h_k\right)_m(r,v_{\parallel},\mu)\,e^{i(m\theta+n\varphi-\omega t)}. \tag{13}$$

Note that we consider safety factor profiles with positive values, where the safety factor is defined as $q=\frac{1}{2\pi}\int_0^{2\pi}(\mathrm{d}\varphi/\mathrm{d}\theta)|_{\text{along }\boldsymbol{B}}\mathrm{d}\theta$. Resonant Fourier modes have phase fronts aligned with the magnetic field lines and verify $nq+m=0$. We typically choose $n<0$, $m>0$. Using equations (11)–(13) and replacing $\boldsymbol{j}$, $\boldsymbol{\delta j}$ and $\boldsymbol{\delta B}$ by their explicit expression, the perpendicular kinetic-MHD momentum conservation equation (5) becomes:

$$\begin{aligned}\sum_k\rho_k\left(-i\omega+(\boldsymbol{u}_{*_k}\cdot\boldsymbol{\nabla})\right)\left(-i\omega\boldsymbol{\xi}_\perp+\frac{\boldsymbol{\nabla}\delta\phi\times\boldsymbol{B}}{B^2}\right)&=\boldsymbol{b}\frac{\mathrm{d}P}{\mathrm{d}r}(\boldsymbol{b}\cdot\boldsymbol{\nabla}\xi_\perp^r)+\sum_k\left[\left(\delta P_{\perp_k}^{\mathrm{tot}}-\delta P_{\parallel_k}^{\mathrm{tot}}\right)\boldsymbol{\kappa}-\boldsymbol{\nabla}_\perp\delta P_{\perp_k}^{\mathrm{tot}}\right]\\&+\frac{1}{\mu_0}(\boldsymbol{\nabla}\times\boldsymbol{B})\times(\boldsymbol{\nabla}\times(\boldsymbol{\xi}_\perp\times\boldsymbol{B}))+\frac{1}{\mu_0}(\boldsymbol{\nabla}\times(\boldsymbol{\nabla}\times(\boldsymbol{\xi}_\perp\times\boldsymbol{B})))\times\boldsymbol{B}.\end{aligned} \tag{14}$$

2.2. Simplified model used in this work and application to cylindrical geometry

Several simplifying assumptions are used from now on. The main reasoning behind those choices is to start with the simplest possible case for testing our new kinetic-MHD code. This makes the benchmarking process easier by having simpler equations to deal with, which significantly simplifies the computation of analytical results for benchmarking purposes. It also simplifies the implementation process and

lowers the numerical cost. These assumptions are detailed below. Nevertheless, the general kinetic-MHD equations and variables as described above will be implemented in our kinetic-MHD code and studied in future work.

Although our kinetic model can treat all the species kinetically, we choose to investigate the case of one kinetic species in this paper. It is numerically expensive to describe all the species kinetically and the dominant kinetic effects are often due to a particular species only. Therefore, from now on, we allow some of the species to be described by the usual MHD fluid treatment, the others being described kinetically. Each considered plasma species can either be described using the fluid equations only or using the hybrid kinetic-MHD model. The index i will be used to describe all the species, kinetic and fluid, the index j will designate the fluid species only and index k will be used to describe the kinetic species. The total pressure is now the sum of the pressure due to non-kinetic and kinetic species, which can be written as:

$$P = \sum_i n_i T_i = \sum_i P_i = \underbrace{\sum_j n_j T_j}_{P_{\text{fluid}}} + \sum_k n_k T_k, \tag{15}$$

where n_i is the number density profile of species i and T_i is its temperature profile.

Only cases where a single species is simulated kinetically are presented in this work. In principle, it can be either bulk ions, minority ions (e.g. generated by neutral beam injection, ion cyclotron resonance heating or α-particles from fusion reactions) or the electrons. In the following, we focus on the case of kinetic minority hot ions, distributed isotropically. The non-kinetic species are simulated only with the standard perpendicular MHD model. The case with multiple kinetic species will be considered in a future publication.

Note that this choice justifies the approximation $\delta\phi \equiv 0$, since the fast ion contribution to the density in (7) is weak. $\delta\phi = 0$ is adopted from now on. This in turn means that the perturbed parallel electric field is zero (see equation (2) and associated discussion, recall that we use a gauge choice where the vector potential has no parallel component). This hypothesis restricts the class of instabilities that can be reproduced by our current code. Note however that many studies of kinetic effects on MHD-like instabilities also neglect this contribution, see e.g. `NOVA-K` for toroidal Alfvén eigenmodes (Chen and Hasegawa 1991) and `MARS-K` for internal kink and resistive wall modes for example (Liu *et al* 2008, 2022). Future work will treat corrections due to this term, in particular those related to the perturbed parallel electric field. Electrostatic effects on internal kink modes due to main ions and electrons were found to be weakly stabilising by Antonsen and Lee (1982). In this work, we focus on the effect of weakly collisional hot minority species on large scale instabilities, such as the internal kink mode. In this case, $\delta\phi = 0$ is an especially good approximation since the kinetic species has a lower density and is much hotter than the thermal population, see e.g. Cheng (1991). Because we have one variable less ($\delta\phi$), the quasi-neutrality equation is no longer necessary. The system of kinetic-MHD equations is therefore constituted only by the momentum equation (14) and the drift-kinetic equation (8). Note that, with $\delta\phi = 0$, the vector $\boldsymbol{\xi}_\perp$, which defines the gauge and vector potential $\boldsymbol{\delta A} = \boldsymbol{\xi}_\perp \times \boldsymbol{B}$, is exactly the perpendicular fluid displacement.

Using $\delta\phi = 0$, and assuming an isotropic hot distribution function, one obtains from equations (6) and (7) for the kinetic species:

$$\delta P^{\text{tot}}_{\perp_k} = -\boldsymbol{\xi}_\perp \cdot \boldsymbol{\nabla} P_k + \delta P_{\perp_k}, \qquad \delta P^{\text{tot}}_{\parallel_k} = -\boldsymbol{\xi}_\perp \cdot \boldsymbol{\nabla} P_k + \delta P_{\parallel_k}, \tag{16}$$

where it was used that the background pressure is isotropic, $P_{\perp_k} = P_{\parallel_k} = P_k$. The kinetic perturbed pressures appearing in (16) are obtained, similarly to (6) as moments of the perturbed distribution, but here only of the kinetic perturbation δh_k:

$$\delta P_{\perp_k} = 2\pi \int_{-\infty}^{\infty} \mathrm{d}v_\parallel \int_0^{\infty} \mathrm{d}\mu\, \mu \frac{B^2}{m_k} \delta h_k, \quad \delta P_{\parallel_k} = 2\pi \int_{-\infty}^{\infty} \mathrm{d}v_\parallel \int_0^{\infty} \mathrm{d}\mu\, v_\parallel^2 B \delta h_k, \tag{17}$$

where δh_k satisfies equation (8). For the non-kinetic species, equation (16) simplifies to $\delta P^{\text{tot}}_{\perp_j} = \delta P^{\text{tot}}_{\parallel_j} = -\boldsymbol{\xi}_\perp \cdot \boldsymbol{\nabla} P_j$. Hence, for the main ions and electrons, the perturbed pressure is almost equal to the ideal MHD result:

$$\delta P_{\text{MHD}} = -\Gamma P \boldsymbol{\nabla} \cdot \boldsymbol{\xi} - \boldsymbol{\xi}_\perp \cdot \boldsymbol{\nabla} P, \tag{18}$$

except the compression term $-\Gamma P \boldsymbol{\nabla} \cdot \boldsymbol{\xi}$ is absent. The suppression of this contribution has essentially no consequence in a cylinder. The main effect of the compression term is to modify the inertia due to

toroidal effects (i.e. $\gamma^2 \to \gamma^2(1+2q^2)$ see for example Graves *et al* (2021) and references therein). Since we are considering a cylinder in this work, this inertial enhancement is absent, and unless far from marginal stability, there is no additional compression effect. In any case, in a torus, the usual MHD inertial enhancement factor associated with MHD compression is much smaller than kinetic inertia associated with the thermal ions (Graves *et al* 2000, Chavdarovski and Zonca 2014). Hence, the parallel component of $\boldsymbol{\xi}$, the term $-\Gamma P \boldsymbol{\nabla}\cdot\boldsymbol{\xi}$, and the parallel momentum equation are usually not required for kinetic-MHD problems (exception being when strong equilibrium flows are accounted for).

The term involving $\boldsymbol{u}_{*_k}$ in the left-hand side of equations (5) and (14) corresponds to diamagnetic corrections due to species k. These effects are not kinetic and in principle appear for all species, regardless of whether they are described kinetically or not. Since we consider exclusively hot minority ions as kinetic particles, their associated diamagnetic corrections are negligible compared to those due to the bulk particles, because $P_k \ll P_{\text{fluid}}$. Moreover, in this work, we also neglect all finite Larmor radius corrections due to the non-kinetic species. This is an approximation that is used to simplify the physical model in view of the benchmarking process and will be lifted in future work.

As mentioned, from now on, we focus on the simplified case of a cylindrical geometry. This is equivalent to considering a tokamak where the major radius is much larger than the minor radius such that the toroidal effects become negligible. We keep r, θ and φ as our three coordinates, where φ now follows the axis of the cylinder. Its length is $L_z = 2\pi R_0$ where R_0 is an equivalent major radius if the cylinder was bent into a torus. This choice implies that in addition to its existing symmetry in the φ direction, the unperturbed system is now also symmetric in the θ direction. As a result, eigenmodes are not only represented by a single Fourier mode n in the toroidal direction, but also by a single Fourier mode m in the poloidal direction. This significantly reduces the number of non-zero elements in the matrices representing the discretised system as defined in equation (31) which means that the numerical cost, both in terms of memory and computation time for iteratively solving the associated generalised eigenvalue problem, is strongly reduced. The cylindrical geometry case has the further advantage that many analytical results can be derived and then used to benchmark the new code. Given $\boldsymbol{\xi}_\perp$ and ω, it is for example possible to solve the drift-kinetic equation exactly for δh_k (see section 4.1). It is also possible to obtain exact analytical expressions for the associated kinetic perturbed pressures. Moreover, in cylindrical geometry, the equilibrium force balance equation (3) can be reduced to a differential equation for a single variable, for example F (see equation (4)), that is sufficient to characterise completely the equilibrium magnetic field. For a known pressure profile (obtained using (15)) and a known safety factor profile, the following differential equation is solved numerically for F in order to obtain the cylindrical equilibrium configuration:

$$\frac{\mathrm{d}F}{\mathrm{d}r} = \frac{rF^2\left(r\frac{\mathrm{d}q}{\mathrm{d}r} - 2q\right) - R_0^4 q^3 \mu_0 \frac{\mathrm{d}P}{\mathrm{d}r}}{qF\left(r^2 + q^2R_0^2\right)}. \tag{19}$$

Using the above assumptions, the kinetic-MHD equations (14), (8) can then be written in cylindrical geometry as:

$$\begin{aligned} -\rho\omega^2\boldsymbol{\xi}_\perp = {} & \frac{1}{\mu_0}(\boldsymbol{\nabla}\times\boldsymbol{B})\times(\boldsymbol{\nabla}\times(\boldsymbol{\xi}_\perp\times\boldsymbol{B})) + \frac{1}{\mu_0}(\boldsymbol{\nabla}\times(\boldsymbol{\nabla}\times(\boldsymbol{\xi}_\perp\times\boldsymbol{B})))\times\boldsymbol{B} \\ & + \boldsymbol{\nabla}(\boldsymbol{\xi}_\perp\cdot\boldsymbol{\nabla}P) + \left(\delta P_{\perp_k} - \delta P_{\parallel_k}\right)\boldsymbol{\kappa} - \boldsymbol{\nabla}_\perp \delta P_{\perp_k}, \end{aligned} \tag{20}$$

$$\left(-i\omega + \boldsymbol{v}_{\boldsymbol{g}_k}\cdot\boldsymbol{\nabla}\right)\delta h_k = -i\left(q_k(\boldsymbol{\xi}_\perp\times\boldsymbol{B})\cdot\boldsymbol{v}_{\boldsymbol{g}_k} - \mu\delta B_\parallel\right)\left(\omega\frac{\partial F_k}{\partial\mathcal{E}} + n\frac{\partial F_k}{\partial P_\varphi}\right). \tag{21}$$

In a cylinder, we have:

$$\boldsymbol{\kappa} = -\frac{rF^2}{q^2R_0^4B^2}\boldsymbol{e}_r, \tag{22}$$

$$\boldsymbol{v}_{\boldsymbol{g}_k}\cdot\boldsymbol{\nabla}\theta = \frac{v_\parallel F}{qR_0^2B} - \frac{m_k v_\parallel^2 F^3}{q_k B^4 q^2 R_0^5} + \frac{\mu F}{2q_k B^3 R_0 r}\frac{\mathrm{d}\left(B^2\right)}{\mathrm{d}r}, \tag{23}$$

$$\boldsymbol{v}_{\boldsymbol{g}_k}\cdot\boldsymbol{\nabla}\varphi = \frac{v_\parallel F}{BR_0^2} + \frac{m_k v_\parallel^2 r^2 F^3}{q_k q^3 B^4 R_0^7} - \frac{\mu r F}{2B^3 q q_k R_0^3}\frac{\mathrm{d}\left(B^2\right)}{\mathrm{d}r}. \tag{24}$$

Notice that the first bracket on the right-hand side of (21) is the Lagrangian associated with the toroidal drift motion of the passing ions and the radial displacement, minus the parallel magnetic field,

i.e. it is the first term in the right hand side of equation (4) in Graves (2013). Later in this paper, benchmarks will adopt the simplified form for $\delta B_{\parallel}$ which in fact cancels the effect of the pressure on the curvature driven drifts, see also Graves (2013). As can be seen in equation (22), the only curvature present in a cylinder is the poloidal curvature. As it is weaker than the toroidal curvature, the kinetic effects are in general smaller in a cylinder than in a torus.

Throughout this work, we will assume a Maxwellian background distribution for the kinetic species, that is:

$$F_k = \left(\frac{m_k}{2\pi T_k}\right)^{3/2} n_k \exp\left[-\frac{m_k v_{\parallel}^2/2 - \mu B}{T_k}\right]. \tag{25}$$

Moreover, we use the following expression for the toroidal momentum:

$$P_\varphi \simeq -q_k \psi \Longrightarrow \frac{\partial F_k}{\partial P_\varphi} = -\frac{1}{q_k}\frac{\partial F_k}{\partial \psi}, \tag{26}$$

where ψ is the poloidal magnetic flux. This expression is exact in the cylinder. In the torus, it means this approximation neglects the banana width correction term in P_φ, though such corrections can be important for certain types of anisotropic populations (see e.g. Graves *et al* (2009)). Finally, in this work, unless specifically mentioned, we consider density and temperature profiles of the form:

$$X(s) = X_0\left(\eta + \Delta\left[\left(\frac{s}{s_{\text{ref}}}\right)^{\nu} - 1\right]^{\mu}\right), \tag{27}$$

where X_0 is a reference quantity in the units of X, $\eta = 0$, $\Delta = -1$, $s_{\text{ref}} = 1.01$, $\nu = 2$, $\mu = 1$. The profile parametrised by these values is monotonically decreasing. Note that using s_{ref} slightly larger than one (for $\eta = 0$) avoids a zero pressure at the edge, which is numerically problematic to handle. As a consequence, the pressure profile of each species, which is obtained by taking the product of the corresponding density and temperature (see equation (15)), follows the same relation except that now $\mu = 2$. Note that we introduced the normalised radial variable s. In the cylinder, $s = r/a$ where a is the minor radius. We consider two different safety factor profiles for this work. The first one corresponds to a resonant case, with the safety factor profile crossing the $q = 1$ rational surface at $s_{\text{res}} = 0.465$). It is given by a profile of the form (27) with $\Delta = -0.78$, $\mu = 1$, $\nu = 3$, $s_{\text{ref}} = -0.709$, $\eta = 0$, $X_0 = 1$. The other profile we use:

$$q_{\text{non-res}}(s) = q_0\left[1 + \left(\left(\frac{q_a}{q_0}\right)^{\nu} - 1\right)s^{2\nu}\right]^{\frac{1}{\nu}}, \tag{28}$$

is a so-called *non-resonant* case which does not cross the $q = 1$ rational surface but approaches it sufficiently to allow an unstable internal kink mode in the low-shear region. In tokamaks, such modes are sometimes referred to as quasi-interchange modes (see e.g. Wesson (1986), Hastie and Hender (1988), Waelbroeck (1989)). We use $q_0 = 1.02$, $q_a = 4$, $\nu = 5$.

Note that the restriction to the functional forms described above for the profiles and the background distribution function are not required by the physical model and the `VENUS-KMHD` code. More general choices for the background distribution function or arbitrary profiles from experimental or numerical results are possible. We only make these choices as a first case to benchmark and test the code. However, the current version of the code only supports isotropic background distributions F_k, for the reasons discussed above.

3. Numerical method

3.1. Expressing the kinetic-MHD equations as a standard eigenvalue problem using the Case–Van Kampen approach

Several techniques exist to solve the coupled kinetic-MHD equations. A common way to approach this kind of problem is to first solve the kinetic equation for δh_k in terms of $\boldsymbol{\xi}_\perp$ and insert the result in the MHD equation via the kinetic perturbed pressure terms. This so-called *Landau approach* is used by several existing kinetic-MHD codes such as `MARS-K` (Liu *et al* 2008), `NOVA-K` (Cheng 1992) or the gyrokinetic code `LIGKA` (Lauber *et al* 2007). It reduces the system of equations to a non-linear eigenvalue problem with eigenvalue ω and the perturbed MHD field $\boldsymbol{\xi}_\perp$ as eigenvector. More specifically, the resulting problem would be of the form $M(\omega)\boldsymbol{\xi}_\perp = 0$, with $M(\omega)$ a non-linear function of ω. The evaluations of the kinetic perturbed pressures in particular invoke an integral over the velocity space that

contains a resonant denominator. These integrals need to carefully address this resonance. In particular, correctly handling the case of damped modes requires carrying out these integrals over appropriate Landau paths. Although this approach is followed successfully by some codes, this is a relatively tedious process that usually involves approximations allowing a simplified semi-analytical approach.

The alternative is the *Case–Van Kampen* approach (Van Kampen 1955, Case 1959), where all the variables, including the perturbed distribution function, are kept for numerical resolution. The downside of this method is that the discretised problem has a very large dimension because the perturbed distribution function, which is now included in the eigenvector, also depends on velocity space. The benefit is that the discretised problem can be written as a linear standard generalised eigenvalue problem, which is easier to handle for numerical resolution. This results in so-called *Case–Van Kampen modes* which are the true eigenmodes of the system. One can show (Bratanov *et al* 2013), that the Case–Van Kampen eigenvalues and eigenvectors coincide with the standard Landau result for unstable modes. Moreover, stable modes can match between the two approaches if finite collisionality is added to the equations (Ng *et al* 1999). In the limit of finite collisionality tending to zero, the collisional Case–Van Kampen spectrum coincides with the collisionless Landau spectrum. Obtaining stable modes in this approach therefore requires the introduction of a dissipation mechanism. Detailed comparisons of the Landau and Case–Van Kampen approaches were performed for example in Bratanov (2011), Bratanov *et al* (2013). Unlike the Landau approach, the Case–Van Kampen approach can straightforwardly be generalised to a time evolution scheme which can then be used to include non-linear physics effects.

Once again following the method used by existing gyrokinetic codes, we propose the use of the Case–Van Kampen approach to express our kinetic-MHD problem. In practice, it consists in including the non-adiabatic fluctuation of the distribution function δh_k in the eigenvector of the system, together with the MHD fields. In this work, we focus on unstable modes, neglecting collisional effects. Being able to express the physical equations as a standard eigenvalue problem is a major advantage in view of the numerical resolution. Linear eigenvalue problems are indeed much easier to handle than non-linear ones and a much greater variety of numerical tools already exists to solve such problems. Similarly, the ideal MHD equations can already be formulated as a linear eigenvalue problem, as used by several existing spectral codes such as `KINX` (Degtyarev *et al* 1997), `CASTOR` (Kerner *et al* 1998), and `VENUS-MHD` (Bustos Ramirez 2023). In the case of this work, the goal is to apply the Case–Van Kampen approach to the hybrid kinetic-MHD equations (20) and (21) expressing the combined system as a linear eigenvalue problem.

Spectral ideal MHD codes typically use $\lambda = -\omega^2$ as the eigenvalue[6], because only second order time derivatives appear in the corresponding equations. On the other hand, $\lambda = -i\omega$ is used as the eigenvalue in spectral gyrokinetic codes because only the first order time derivative appears in the associated equations. In the case of the kinetic-MHD system (20) and (21), both ω and ω^2 appear in the equations, which at first sight would lead to a non-linear eigenvalue problem in ω. To avoid this difficulty, we introduce an extra variable $\boldsymbol{\delta u}_\perp$, the perturbed fluid velocity. Taking into account the simplifications considered for this work, it is linked to the MHD displacement $\boldsymbol{\xi}_\perp$ simply by:

$$-i\omega\boldsymbol{\xi}_\perp = \boldsymbol{\delta u}_\perp. \tag{29}$$

As equilibrium flows are not yet included in this work, the full fluid velocity is simply given by $\boldsymbol{u} = \boldsymbol{\delta u}_\perp$. We now take advantage of this extra variable to remove the second time derivative in equation (20), by replacing $-\omega^2\boldsymbol{\xi}_\perp$ by $-i\omega\boldsymbol{\delta u}_\perp$. Equation (20) modified in this way along with equations (21) and (29) can be written as a generalised standard eigenvalue problem of the form:

$$A\begin{pmatrix}\boldsymbol{\xi}_\perp\\ \boldsymbol{\delta u}_\perp\\ \delta h_k\end{pmatrix} = -i\omega B\begin{pmatrix}\boldsymbol{\xi}_\perp\\ \boldsymbol{\delta u}_\perp\\ \delta h_k\end{pmatrix} \Longleftrightarrow A\boldsymbol{x} = \lambda B\boldsymbol{x}, \tag{30}$$

where $\lambda = -i\omega$ is the numerical eigenvalue and $\boldsymbol{x} = (\boldsymbol{\xi}_\perp, \boldsymbol{\delta u}_\perp, \delta h_k)^\intercal$ is an abstract notation for our vector of unknowns. The crucial point is that the matrices A and B do not depend on ω thanks to the Case–Van Kampen formulation. The matrix A and B write:

$$A = \begin{pmatrix}A_{11} & 0 & A_{13}\\ 0 & 1 & 0\\ A_{31} & 0 & A_{33}\end{pmatrix}, \quad B = \begin{pmatrix}0 & \rho & 0\\ 1 & 0 & 0\\ B_{31} & 0 & 1\end{pmatrix}, \tag{31}$$

[6] Note that in this section, λ denotes an eigenvalue, not the pitch angle.

with:

$$A_{11} = (\nabla \times \boldsymbol{B}) \times (\nabla \times (\bullet \times \boldsymbol{B}))/\mu_0 + (\nabla \times (\nabla \times (\bullet \times \boldsymbol{B}))) \times \boldsymbol{B}/\mu_0 + \nabla (\bullet \cdot \nabla P), \tag{32}$$

$$A_{13} = 2\pi \boldsymbol{\kappa} \int_{-\infty}^{\infty} \mathrm{d}v_{\parallel} \int_{0}^{\infty} \mathrm{d}\mu (\bullet) \left(\frac{\mu B^2}{m_k} - v_{\parallel}^2 \right) - \nabla_{\perp} \left(2\pi \int_{-\infty}^{\infty} \mathrm{d}v_{\parallel} \int_{0}^{\infty} \mathrm{d}\mu (\bullet) \frac{B^2 \mu}{m_k} \right), \tag{33}$$

$$A_{31} = -in \left[q_k (\bullet \times \boldsymbol{B}) \cdot \boldsymbol{v}_{\boldsymbol{g}_k} - \mu (\nabla \times (\bullet \times \boldsymbol{B})) \cdot \boldsymbol{b} \right] \frac{\partial F_k}{\partial P_{\varphi}}, \tag{34}$$

$$A_{33} = -\boldsymbol{v}_{\boldsymbol{g}_k} \cdot \nabla, \tag{35}$$

$$B_{31} = -\left[q_k (\bullet \times \boldsymbol{B}) \cdot \boldsymbol{v}_{\boldsymbol{g}_k} - \mu (\nabla \times (\bullet \times \boldsymbol{B})) \cdot \boldsymbol{b} \right] \frac{\partial F_k}{\partial \mathcal{E}}, \tag{36}$$

where the dots • indicate where the corresponding variable enters in the equation. This is however a formal notation since the components of $\boldsymbol{x}$ still need to be discretised over configuration space. Furthermore, δh_k also needs to be discretised on velocity space using finite differences.

Note that this structure is preserved when generalising the equations to include multiple kinetic species, equilibrium flows or non-zero perturbed electrostatic potential. For example, in the case of n kinetic species, we have $\boldsymbol{x} = (\boldsymbol{\xi}_{\perp}, \boldsymbol{\delta u}_{\perp}, \delta h_1, \ldots, \delta h_k, \ldots, \delta h_n)$. If corrections due to the electrostatic potential are included, $\delta\phi$ (see equation (2)) has to be added to the variables of the problem and an extra equation, the quasi-neutrality equation (10), needs be included in the kinetic-MHD system of equations. Note that due to the presence of the B matrix in front of the eigenvalue λ with B different from the identity matrix, this is a *generalised* linear eigenvalue problem, not the standard formulation. Unlike the linearised ideal MHD problem or gyrokinetic equation, which can be formulated as a standard linear eigenvalue problem (see for example Jenko *et al* (2000), Bustos Ramirez (2023)), the generalised form is necessary in the kinetic-MHD case. This is a minor complication as many algorithms and existing numerical libraries that solve standard linear eigenvalue problems can handle the generalised formulation as well. Note that if, as in our case, the B matrix is invertible, it is sufficient to multiply (30) by B^{-1} on the left to transform the generalised eigenvalue problem into a standard one.

3.2. The `VENUS-KMHD` code

Although this work focuses on cylindrical geometry, we present here the numerical methods in the general case. The numerical part of this work is an extension of the existing `VENUS-MHD` code (Lanthaler 2020, Bustos Ramirez 2023), which is a linear ideal MHD stability spectral code. It is written using a modular structure that allows to solve any stability problem in toroidal or cylindrical geometry that can be written as a generalised eigenvalue problem $A\boldsymbol{x} = \lambda B\boldsymbol{x}$. Many ideal MHD models, with and without the parallel dynamic as well as with and without flows, can be written in this form and several are readily available in the `VENUS-KMHD` framework. The physical model to be used is chosen at run time.

In practice, the main part of the `VENUS-MHD` code is written in Python. Following the work of Lanthaler (2020), a `Mathematica` routine (Wolfram Research, Inc. 2017) is used to compute the weak form of the physical equations in a finite element discretisation approach, compute each component of the vector equations including geometrical factors, express the result in the form of a generalised standard eigenvalue problem and write the corresponding Python code. This allows us to easily change the definition of the numerical variables if necessary and to significantly simplify the modification of the physical model, for example when including a new physical effect. It also strongly mitigates the risk of error when implementing long expressions.

An equilibrium configuration is required as part of the input. It can be obtained using an analytical relation (e.g. toroidal equilibrium from Solov'ev (1968), cylindrical equilibrium from Gruber and Rappaz (2012) or equation (19)) or with a numerical code (currently `VMEC` (Hirshman and Whitson 1983) is used). The problem is discretised in space and the matrix elements of A and B are computed. An external library is then called to solve the standard eigenvalue problem and obtain the physically most unstable eigenmode, i.e. the associated eigenvalue and eigenvector. Although it is significantly more expensive numerically, one can in addition request a few of the first subdominant modes.

The poloidal and toroidal dependence of all physical dependent variables is discretised using Fourier modes, as described in section 2 as well as equations (11) and (13). The radial direction is discretised using finite elements, B-Splines are used. Their degree can differ for representing the different physical variables and can be chosen at run time. In practice, one typically uses an order of one more for the two radial variables $\xi_{\perp}^{r}$ and $\delta u_{\perp}^{r}$ than for the others. This permits the incompressibility condition that involves $\nabla \cdot \boldsymbol{\xi}_{\perp}$ as well as the $\nabla \cdot \boldsymbol{\delta B} = 0$ condition to be exactly satisfied, as these relations only involve finite elements of the same order. Indeed, these conditions include a derivative in the radial direction (which decreases the degree of the corresponding finite element by one) and a derivative in the poloidal

direction (which leaves the degree of the radial finite element unchanged). This choice avoids the so-called *spectral pollution* phenomenon that can arise otherwise (Gruber and Rappaz 2012).

The approach used by VENUS-MHD is then generalised to include kinetic effects. We call the resulting enhanced code VENUS-KMHD. As already explained in section 3.1, the kinetic-MHD problem can be expressed as a generalised standard eigenvalue problem using the Case–Van Kampen approach. This is precisely the type of stability equation that can be solved by the VENUS-MHD code. The generation of the equilibrium as well as the handling of the spatial discretisation can be reused unchanged. We make sure that ideal results can also still be obtained with VENUS-KMHD, thus ensuring the code is back-compatible.

The main difference of the kinetic-MHD case compared to ideal MHD is that one of the variables in $\boldsymbol{x}$ (see equation (30)), δh_k, depends not only on space r, θ, φ, but also on a two-dimensional velocity space parametrised by the variables $v_\parallel$ and μ (see section 2). The infinite velocity space is approximated to $-v_{\max} \leqslant v_\parallel \leqslant v_{\max}$ and $0 \leqslant \mu \leqslant \frac{m_k v_{\max}^2}{2B}$. Numerically, normalised variables are used with $\hat{v}_\parallel = v_\parallel / v_{\mathrm{th}_k}$, where $v_{\mathrm{th}_k} = \sqrt{T_k(0)/m_k}$. Similarly, we use $\hat{\mu} = \mu(B_{\mathrm{ref}}/T_k(0))$, where B_{ref} is the reference magnetic field, typically 1 T in this work. Moreover, we use $v_{\max}/v_{\mathrm{th}_k} \cong 6$. The velocity space is discretised using a two-dimensional grid containing $N_{v_\parallel}$ points in the $v_\parallel$ direction and N_μ points in the μ direction. Note that since we consider only cylindrical geometry in this work, we do not need to worry about resolving correctly the passing/trapped boundary, as there are no trapped particles in a cylinder. However, this kind of velocity discretisation has been used successfully in toroidal geometry by several gyrokinetic codes (for example GENE, Jenko *et al* (2000)).

We start by discretising δh_k over velocity space, which maps our five original variables to a collection of $4 + N_{v_\parallel} N_\mu$ variables that depend only on real space:

$$\begin{aligned}(\xi_\perp^r, \xi_\perp^\perp, \delta u_\perp^r, \delta u_\perp^\perp, \delta h_k(v_{\parallel_1}, \mu_1), \cdots, \delta h_k(v_{\parallel_1}, \mu_{N_\mu}),\\ \delta h_k(v_{\parallel_2}, \mu_1), \cdots, \delta h_k(v_{\parallel_2}, \mu_{N_\mu}),\\ \vdots\\ \delta h_k(v_{\parallel_{N_{v_\parallel}}}, \mu_1), \cdots, \delta h_k(v_{\parallel_{N_{v_\parallel}}}, \mu_{N_\mu})).\end{aligned} \tag{37}$$

In the general case of k kinetic species, the kinetic-MHD problem would thus require $4 + kN_{v_\parallel} N_\mu$ variables that depend only on space. The considered grid is regular in the $v_\parallel$ direction with step size $\Delta v_\parallel$. The derivatives in this variable are evaluated using a fourth-order finite difference formula:

$$\frac{\partial \delta h_k}{\partial v_\parallel}\left(v_{\parallel_l}\right) = \frac{\delta h_k\left(v_{\parallel_{l-2}}\right) - 8\delta h_k\left(v_{\parallel_{l-1}}\right) + 8\delta h_k\left(v_{\parallel_{l+1}}\right) - \delta h_k\left(v_{\parallel_{l+2}}\right)}{12\Delta v_\parallel} + \mathcal{O}\left(\Delta v_\parallel^4\right). \tag{38}$$

Note that there is no derivative in $v_\parallel$ appearing in the equations in cylindrical geometry because $\boldsymbol{b} \cdot \boldsymbol{\nabla} B = 0$ and $\boldsymbol{\kappa} \cdot \boldsymbol{v}_{\boldsymbol{g}_k} = 0$. Dirichlet boundary conditions are used for δh_k in the velocity space. When evaluating derivatives in $v_\parallel$, values of δh_k outside of considered velocity domain are taken to be zero. As the distribution functions tend to zero at $v_\parallel, v_\perp \to \pm\infty$, this is equivalent to neglecting the small non-zero contribution of the tail of the distribution function between the numerical boundary of the velocity domain and infinity. The velocity grid in the μ direction, which is a constant of motion and can therefore be handled as a parameter, can either be regular in μ or irregular such that it is regular in $v_\perp$ ($\propto \sqrt{\mu}$). The latter option is the standard due to its observed faster convergence rate and will be used throughout this work. The kinetic perturbed pressures are computed by numerically integrating the discretised δh_k on the (finite) discretised velocity space, using the trapezoidal rule.

The matrices A and B have a three level block structure. The lowest level corresponds to the radial discretisation, the second level to the poloidal modes. The highest level is associated with the collection of variables (presented in the perpendicular kinetic-MHD case in equation (37)) which in the case of VENUS-KMHD also contains the velocity space discretisation. This level of the block structure is characterised by a small full matrix (32) corresponding to the ideal MHD part of the equations, a few sets of full rows and columns corresponding to the kinetic-MHD coupling terms (kinetic pressures in the MHD momentum equation (33) and perturbed Lagrangian in the drift-kinetic equations (34) and (36)) and a multidiagonal part (35) corresponding to the purely kinetic part of the equation. Its multidiagonal form is a consequence of the finite difference formula (38). Overall, because $N_{v_\parallel} N_\mu \gg 4$, two of the three block levels of the matrices are sparse. Furthermore, in cylindrical geometry, the non-sparse level related to the number of considered poloidal modes is reduced to a single element because a single mode is sufficient. Because the blocks associated with the poloidal modes are dense, this provides a drastic reduction of the number of non-zero elements in the matrices, although the number of poloidal modes necessary in tokamak geometry is of the order of 10 only.

In order to have a reasonable resolution in velocity grid, the number of variables for the kinetic-MHD model, $4 + N_{v_\parallel} N_\mu$, will be much larger than the number of variables typically used in ideal MHD models in `VENUS-MHD`, which is at most eight (for example in the case of some models with flows). Because of this, some numerical challenges arise in `VENUS-KMHD` where no problem appeared in the corresponding situation in `VENUS-MHD`. The two matrices A and B are much larger in kinetic-MHD which means the computational requirements are higher, in particular in memory.

To address this issue, a parallel version of the code was developed. The parallelisation is done through `MPI` and more specifically its Python implementation `mpi4py` (Dalcin *et al* 2011). The sparse matrices are stored using the `PETSc` library (Balay *et al* 1997, 2022). The eigenvalue solver is provided by the `SLEPc` library (Hernandez *et al* 2005), natively coupled with `PETSc`. Once again it is the Python wrappers `petsc4py` and `slepc4py` that are used in practice. The parallelisation of the eigenvalue solver and all the communications related to the splitting of the matrices over several processes are handled entirely by the libraries. The matrices are divided over each `MPI` process by rows, each process owns a few (entire) rows of the matrices A and B. The number of rows owned by each process is in general not evenly spread and is determined such that the number of non-zero elements stored by each process is approximately similar. It is still possible to use `SciPy` sparse matrices as well as `SciPy`'s wrapper of `ARPACK` as the eigenvalue solver (as done in `VENUS-MHD`), but only in serial execution.

Numerically, both the ideal MHD and the kinetic-MHD spectral problems are characterised by a large spectrum aspect ratio. We define the spectrum aspect ratio as $\max(|\Im(\lambda)|)/\max(|\Re(\lambda)|)$, where $\Re$ and $\Im$ denote the real and imaginary part of a complex number respectively. This number is typically comprised between 10^5 and 10^6 in physically relevant cases. The modes of physical interest, which are the most unstable ones, correspond to the eigenvalues with the largest real part (recall that $\lambda = -i\omega$). Moreover, the eigenvalues associated with the physical modes are very close to the real axis, because their real frequency is of the same order as the growth rate or smaller. As a consequence, because of the large aspect ratio of the spectrum, the physical modes are very much subdominant in magnitude. Therefore, although they are located at the periphery of the spectrum, the most common eigenvalue solvers are unable to find them because in terms of magnitude, they are in the interior of the spectrum. Careful selection of the numerical method is therefore required in order to be able to obtain these modes. We use either the Krylov–Schur (Hernandez *et al* 2007) eigenvalue solver with a shift-invert transformation or the generalised Davidson solver (Romero and Roman 2014). The challenges associated with identifying the dominant mode in the kinetic-MHD problem as well as further details concerning the different solving options available in `VENUS-KMHD` and convergence studies will be detailed in a future publication.

4. Benchmarks in cylindrical geometry

In this section, several benchmarks will be performed where the `VENUS-KMHD` code will be compared with newly derived analytical relations. We consider the kinetic effects of minority hot α particles following a Maxwellian equilibrium distribution function. The kinetic hot particles are described using the same temperature and density profiles as the main ions and electrons. We use $N_r = 200$, $N_m = 1$, $N_{v_\parallel} = 64$, $N_\mu = 32$, $T_k/T_{\text{bulk}} = 50$, $n_k/n_{\text{bulk}} = 0.033$. We consider an $n = 1$, $m = 1$ internal kink mode both with a resonant and a non-resonant safety factor profile. Note that this corresponds to a $m = 1$, $n = -1$ kink mode in the convention used by `VENUS-KMHD`; however, here it will be referred to as a $n = m = 1$ kink mode in order to avoid highlighting the peculiarities of codes that are based on left-handed coordinates (e.g. `VMEC`). The ideal MHD structure of the considered internal kink modes is shown in figure 1. In the resonant case, the mode is destabilised by both pressure effects and current effects in the inner region where $q < 1$. On the other hand, when the non-resonant $q-$profile (28) is used, the current effects are stabilising everywhere, since q is always greater than one. However, in the low shear region, they are small enough to enable a pressure-driven internal kink mode to develop, if the pressure gradient is sufficiently strong. Since the two physical effects are competing in this case, a very weakly unstable mode is obtained. The different assumptions considered in the following subsections when obtaining analytical relations for benchmarking are summarised in table 1. Note that because we use a linear approach to solve the kinetic-MHD equations, the norm and the phase of the eigenvector and therefore of $\boldsymbol{\delta u}_\perp, \boldsymbol{\xi}_\perp$ and δh_k has no physical meaning and can change between runs of the same physical case. We choose the norm and the phase of the eigenvector by imposing that $\xi^r_\perp$ is equal to 1 and has no imaginary part at the magnetic axis. This choice will be applied throughout this work.

On the technical side, these simulations are typically performed using the generalised Davidson eigenvalue solver, except the simulations in the low frequency limit (see section 4.3.1) where we use the Krylov–Schur eigenvalue solver with direct shift-invert using a LU decomposition. In all cases, only the most unstable mode is requested and studied. These simulations can run on a standard computer. With

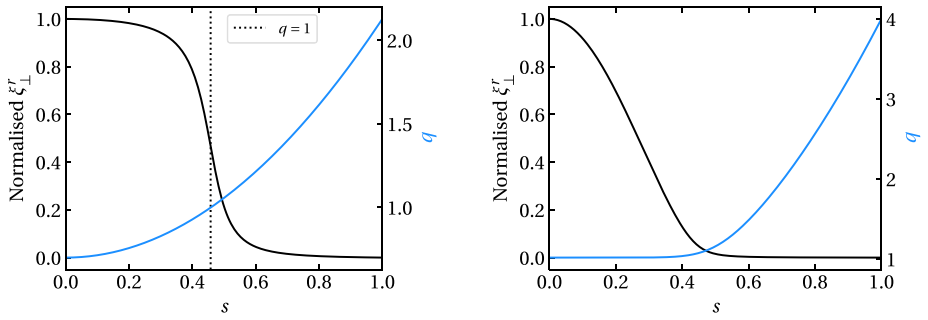


Figure 1. Structure of the considered internal kink mode here for $\xi^r_\perp$ as a function of the normalised radial variable for a resonant (*left*) and a non-resonant (*right*) $q-$profile, here without kinetic effects. In the resonant case, the dotted line shows the location of the $q = 1$ rational surface. The $q-$profile is also shown (in blue).

Table 1. Summary of the different assumptions used throughout this work when solving the drift-kinetic equation (21) to obtain semi-analytical results used to benchmark the code. The approximations that are not applied consistently in `VENUS-KMHD` when benchmarking are detailed in the notes below the table. In these cases, we expect the numerical and analytical results to agree if $\Delta q \ll 1$, that is q is very close to 1 in the inner region. Note that in section 5, no analytical computation will be considered and all the physical effects, including $\delta B_\parallel$, will be included without approximation.

Section	$-i\omega\delta h_k$	$(\boldsymbol{v}_{\boldsymbol{g}_k}\cdot\boldsymbol{\nabla})\delta h_k$	$\left(q_k(\boldsymbol{\xi}_\perp\times\boldsymbol{B})\cdot\boldsymbol{v}_{\boldsymbol{g}_k}-\mu\delta B_\parallel\right)$	$\omega\frac{\partial F_k}{\partial\mathcal{E}}$	$n\frac{\partial F_k}{\partial P_\varphi}$
4.1	Yes	Yes	$\delta B_\parallel \approx$ (41)	Yes	Yes
4.2.2	Yes	$\approx n(\omega_d^\varphi + \Delta q\dot{\theta}_0)\delta h_k^{1,2}$	$\approx \frac{B_0 r q_k \omega_{d0}^\varphi \xi^r_\perp}{q}{}^{1,3}$	Yes	Yes
4.2.3	Yes	$\approx v_\parallel(\boldsymbol{b}\cdot\boldsymbol{\nabla})\delta h_k$	No $\delta B_\parallel$	Yes	Yes
4.3.1[5]	No	$\approx n\omega_d^\varphi\delta h_k^{1,4}$	$\approx \frac{B_0 r q_k \omega_{d0}^\varphi \xi^r_\perp}{q}{}^{1,3}$	No	Yes
4.3.2[5]	Yes	No	$\delta B_\parallel \approx$ (41)	Yes	No

[1] For notations, see section 4.2.1.

[2] No approximation in `VENUS-KMHD`.

[3] No approximation in `VENUS-KMHD`, except that approximation (41) for $\delta B_\parallel$ is used, as in the analytical derivation.

[4] In `VENUS-KMHD`, $(\boldsymbol{v}_{\boldsymbol{d}_k}\cdot\boldsymbol{\nabla})\delta h_k$ is used, see equation (9).

[5] Assumptions used when deriving the governing equations but not in the `VENUS-KMHD` runs: expansion in large aspect ratio, $F' =$ (19), $F = R_0B_0$, $\mathrm{d}q/\mathrm{d}r$ is neglected (assumed of higher order in $\epsilon = r/R_0$).

the standard resolution given above, they require approximately 30 GB of memory and of the order of a few hundred to a few thousands seconds depending on the case to reach solution.

In section 4.1, we analytically solve the drift-kinetic equation in cylindrical geometry and use this expression to benchmark the `VENUS-KMHD` code. In section 4.2, in addition to analytically solving the drift-kinetic equation, we obtain analytical expressions for the kinetic perturbed pressures $\delta P_{\perp_k}$, $\delta P_{\parallel_k}$. Those are not complete analytical solutions of the kinetic-MHD equations, but are exact relations that give us $\delta P_{\perp_k}$, $\delta P_{\parallel_k}$ as a function of the radius for known MHD variables $\boldsymbol{\xi}_\perp$ and ω. We will use energy and pitch angle as the velocity space variables and obtain expressions for the kinetic perturbed pressures that simply require a numerical integration on the pitch angle. We then note that under some approximations, it is possible to obtain fully analytical relations for $\delta P_{\perp_k}$, $\delta P_{\parallel_k}$ if we use the parallel velocity and the magnetic moment as the velocity variables.

4.1. Benchmark of the distribution function

We start the series of benchmarks by verifying that the solution of the drift-kinetic equation obtained by the code is correct. To check this, we consider a cylindrical geometry for which the drift-kinetic equation (21) can actually be analytically solved. In this geometry, it reads:

$$\left[-\omega+\frac{v_\parallel F}{qBR_0^2}(m+nq)+\frac{F}{R_0 r q_k q B^4}\left(\frac{m_k v_\parallel^2 r F^2}{q^2R_0^4}-\frac{\mu B}{2}\frac{\mathrm{d}\left(B^2\right)}{\mathrm{d}r}\right)\left(\left(\frac{r}{R_0}\right)^2 n-mq\right)\right]\delta h_k$$
$$=\delta\mathcal{L}\left[\frac{n}{q_k}\left(\frac{1}{n_k}\frac{\mathrm{d}n_k}{\mathrm{d}\psi}+\left(\frac{m_k v_\parallel^2}{2}+\mu B\right)\frac{1}{T_k^2}\frac{\mathrm{d}T_k}{\mathrm{d}\psi}-\frac{3}{2T_k}\frac{\mathrm{d}T_k}{\mathrm{d}\psi}\right)+\frac{\omega}{T_k}\right]F_k, \tag{39}$$

where we used (9), (15), (26), (23), (24) and we replaced the derivatives of F_k by their explicit expression for the Maxwellian (25). The perturbed Lagrangian $\delta\mathcal{L}$ in a cylinder is given by:

$$\delta\mathcal{L} = \left[\frac{\xi_\perp^r}{B^2}\left(\frac{m_k v_\parallel^2 r F^{\,2}}{q^2 R_0^4} - \frac{\mu B}{2}\frac{\mathrm{d}\left(B^2\right)}{\mathrm{d}r}\right) - \mu\delta B_\parallel\right]. \tag{40}$$

Following Graves *et al* (2019), we use the following approximation:

$$\delta B_\parallel = -\frac{\mu_0 \delta P^{\mathrm{tot}}_{\perp_k}}{B} \simeq \frac{\xi_\perp^r}{B_0}\mu_0\frac{\mathrm{d}P}{\mathrm{d}r}, \tag{41}$$

where we neglected the kinetic contribution in $\delta P^{\mathrm{tot}}_{\perp_k}$, see equation (16). This approximation can be obtained from the perpendicular component of Ampère's law, see also e.g. Antonsen and Lane (1980), Chen and Hasegawa (1991), Zonca and Chen (2006) and can be interpreted as the perpendicular pressure balance with kinetic corrections to $\delta P_\perp$ omitted. This approximation is not necessary at this point, but it will be very useful later to simplify the analytical developments. Note that this approximation was observed to be good in most cases in the physical situations we considered. However, as will be discussed below, this approximation is also used in VENUS-KMHD when the goal is to benchmark it against analytical derivations that use (41). For this reason, it is not critical to ensure that this approximation is valid physically since we apply it consistently in the two results we aim to compare. Nevertheless, its validity domain will be briefly discussed in the two limits considered in sections 4.3.1 and 4.3.2. We also need to express the derivatives with respect to ψ as derivatives in r before continuing. Using $\psi = -R_0 A_\varphi$ and $rF/(qR_0^2) = -\mathrm{d}A_\varphi/\mathrm{d}r$, we find $\mathrm{d}\psi/\mathrm{d}r = rF/(qR_0)$. Using this result and (41), we find:

$$\delta h_k = \frac{\xi_\perp^r \delta\mathcal{L}\left[\frac{R_0 nq}{rFq_k}\left(\frac{1}{n_k}\frac{\mathrm{d}n_k}{\mathrm{d}r} + \left(\frac{m_k v_\parallel^2}{2} + \mu B\right)\frac{1}{T_k^2}\frac{\mathrm{d}T_k}{\mathrm{d}r} - \frac{3}{2T_k}\frac{\mathrm{d}T_k}{\mathrm{d}r}\right) + \frac{\omega}{T_k}\right]F_k}{\left[-\omega + \frac{v_\parallel F}{qBR_0^2}(m+nq) + \frac{F}{R_0 r q_k q B^4}\left(\frac{m_k v_\parallel^2 r F^{\,2}}{q^2 R_0^4} - \frac{\mu B}{2}\frac{\mathrm{d}(B^2)}{\mathrm{d}r}\right)\left(\left(\frac{r}{R_0}\right)^2 n - mq\right)\right]}. \tag{42}$$

It is now possible to use this expression to test the code. Knowing the input profiles, the equilibrium and the result for $\boldsymbol{\xi}_\perp$ and ω, one can then compute the corresponding analytical solution for δh_k using (42) and compare with the numerical solution for δh_k. Two examples are presented in figure 2 for the resonant and non-resonant physical cases of figure 1. In each case, two VENUS-KMHD simulations are presented, one using the exact expression for $\delta B_\parallel$ and one using approximation (41), which was also used to obtain the analytical solution (42). In the latter case, one observes excellent agreement, even for the resonant case which includes fine-scale structures. Those abrupt variations of δh_k are due to wave-particle resonances, as will be discussed in section 5. It is important to note that since we used the approximation (41) for $\delta B_\parallel$, for closest benchmark, it is necessary to use the same approximation in VENUS-KMHD as well. On the other hand, it appears clearly that when the exact expression for $\delta B_\parallel$ is used in the code, a significant discrepancy is observed. As a consequence, for the rest of the benchmarks, approximation (41) will be used in the code in order to correspond to the method used to obtain the analytical relations.

4.2. Benchmark of the kinetic perturbed pressures: general case

4.2.1. Introduction and notations

Now that it was shown that the VENUS-KMHD code correctly solves the drift-kinetic equation, one can do a further analytical test and see if the kinetic perturbed pressures $\delta P_{\perp_k}, \delta P_{\parallel_k}$ are correctly reproduced. The general idea is the same as before: first a self-consistent kinetic-MHD solution is computed with VENUS-KMHD, then the profiles as well as the numerical results for ω and $\boldsymbol{\xi}_\perp$ are used as input for the analytical relation. When we compare the pressure, one also needs to compute the numerical perturbed pressures from the numerical δh_k provided by the code. This is done by using the same two-dimensional trapezoidal rule to compute (17) on the discretised velocity grid as used by VENUS-KMHD. For the analytical derivation that follows, unlike what was done above, we use as velocity variables $\mathcal{E}$ and $\lambda = \mu/\mathcal{E}$, which are more convenient for analytical work. We introduce the following new notations (see e.g. Graves (2013)) that were used for this derivation as it is more convenient for this computation and would allow a straightforward generalisation to the toroidal case:

$$\omega_d^\varphi = \boldsymbol{v}_{\boldsymbol{g}_k}\cdot(\boldsymbol{\nabla}\varphi - q\boldsymbol{\nabla}\theta) \cong \frac{\mathcal{E}}{q_k}\left(\frac{2-\lambda B}{BR_0^2 q} + \frac{\lambda q\mu_0}{rB^2}\frac{\mathrm{d}P}{\mathrm{d}r}\right), \quad \dot{\theta}_0 = \frac{v_\parallel}{qR_0}, \quad \Delta q = q + m/n. \tag{43}$$

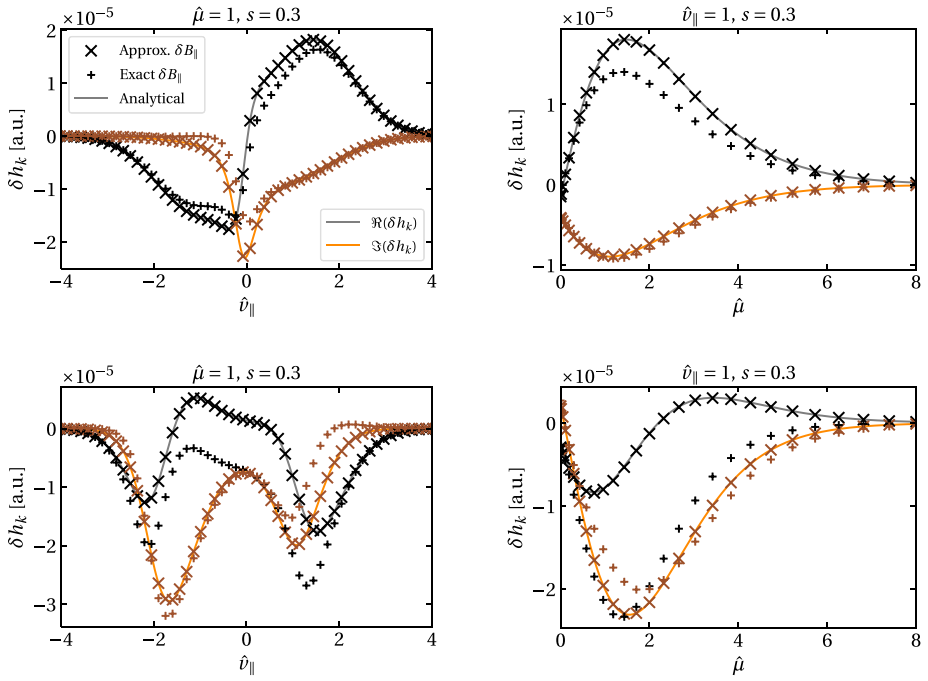


Figure 2. Analytical (solid line) and numerical (points) result for the kinetic perturbed distribution function for a resonant (*top row*) and a non-resonant (*bottom row*) safety factor profile. In the analytical solution as well as in the case of the numerical results denoted by crosses, approximation (41) for $\delta B_\parallel$ is used while for the numerical results denoted by the + markers, the exact expression is used. The real part (black) and the imaginary part (orange) are shown. Cuts in the velocity space are shown, we fix $\hat{\mu} = 1$ (*left column*) and $\hat{v}_\parallel = 1$ (*right column*) at $s = 0.3$ (in both cases).

Using once again (41), we also introduce:

$$\omega_{d0}^{\varphi} = \omega_d^{\varphi} - \frac{q\mu\delta B_\parallel}{q_k B_0 r \xi_\perp^r} \cong \frac{1}{R_0^2 q \Omega_{c_k}} \left(v_\parallel^2 + \frac{\mu B}{m_k} \right) = \mathcal{E} \frac{2 - \lambda B}{q_k B R_0^2 q}. \tag{44}$$

Using these new notations, the drift-kinetic equation (21) can be rewritten as:

$$\left[\omega + n \left(\omega_d^{\varphi} + \Delta q \dot{\theta}_0 \right) \right] \delta h_k = \frac{B_0 r q_k \omega_{d0}^{\varphi} \xi_\perp^r}{q} \left(\omega + n\omega_* \right) \frac{\partial F_k}{\partial \mathcal{E}}, \tag{45}$$

where $\omega_* = -\left(\frac{q}{q_k} \frac{\partial F_k}{\partial \psi} \right) / \left(\frac{\partial F_k}{\partial \mathcal{E}} \right)$. Note that because there are no radial drifts in cylindrical geometry, no ω_d^{ψ} term appears in the equation, unlike what is observed in the toroidal computation of Graves (2013) for example. A consequence of this is that, in a cylinder, the drift-kinetic equation only involves the radial component of the displacement. The solution for δh_k is straightforward to obtain from (45):

$$\delta h_k = \frac{B_0 r q_k \omega_{d0}^{\varphi} \xi_\perp^r}{q \left[\omega + n \left(\omega_d^{\varphi} + \Delta q \dot{\theta}_0 \right) \right]} \left(\omega + n\omega_* \right) \frac{\partial F_k}{\partial \mathcal{E}}. \tag{46}$$

4.2.2. Computation of the perturbed kinetic pressures

Knowing the analytical solution of the drift-kinetic equation, it is now possible to compute the kinetic perturbed pressures. In the $(\mathcal{E}, \lambda)$ velocity variables, the kinetic pressures (17) write:

$$\delta P_{\perp_k} = \frac{2\pi}{2m_k^3} \sum_\sigma \int_0^\infty \mathrm{d}\mathcal{E} \mathcal{E}^{3/2} \int_0^{1/B} \mathrm{d}\lambda \frac{\lambda B^2}{\sqrt{1 - \lambda B}} \delta h_k, \tag{47}$$

$$\delta P_{\parallel_k} = \frac{4\pi}{\sqrt{2m_k^3}} \sum_\sigma \int_0^\infty \mathrm{d}\mathcal{E} \mathcal{E}^{3/2} \int_0^{1/B} \mathrm{d}\lambda B \sqrt{1 - \lambda B} \delta h_k. \tag{48}$$

We compute the perturbed pressures using equations (46)–(48). The integral on $\mathcal{E}$ can be performed analytically, we find:

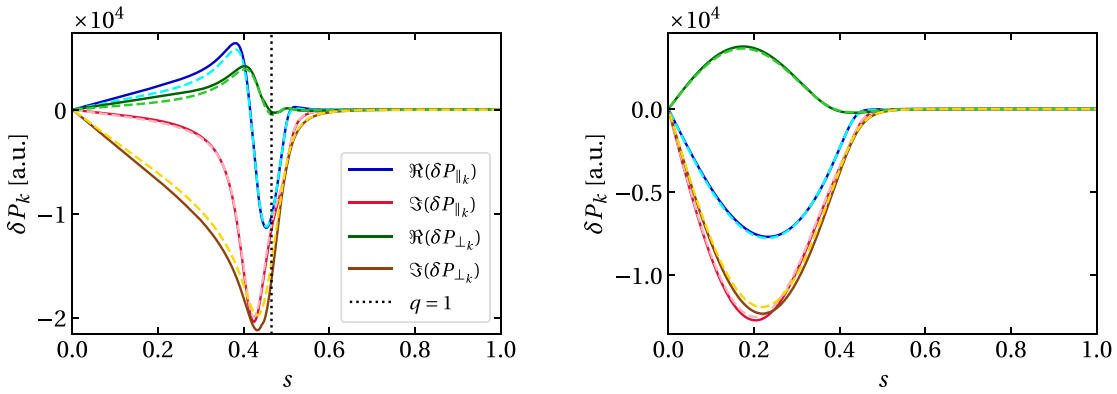


Figure 3. Comparison of the kinetic perturbed pressures $\delta P_{\perp_k}, \delta P_{\parallel_k}$ obtained with `VENUS-KMHD` (dashed lines) using approximation (41) for $\delta B_\parallel$ and with the analytical relations (49) and (50) (solid lines). In each case, the real and the imaginary parts are shown. The MHD displacement and the growth rate used in the analytical relations are taken from the numerical result. A resonant-case (*left*) and a non-resonant case (*right*) are shown. For the former, the rational surface $q = 1$ associated with the considered $n = m = 1$ internal kink mode is shown by the vertical dotted line.

$$\delta P_{\perp_k} = \frac{n_k}{T_k^{3/2}} \frac{B_0 r}{q} \xi_\perp^r \int_0^{1/B} \mathrm{d}\lambda \frac{\lambda B^2}{\sqrt{1-\lambda B}} \left(\frac{2-\lambda B}{BR^2 q}\right) \times \left[\left(\frac{-4}{\tilde{\omega}_d^\varphi}\right)\left(\frac{1}{x_1+x_2}\right)\left(\omega_1 T_k^{7/2}\left(\frac{3}{4}(x_1+x_2)+\frac{1}{2}(x_1^3+x_2^3)+(x_1^5+x_2^5)+x_1^6 Z(x_1)+x_2^6 Z(x_2)\right)\right.\right. \left.\left. + \omega_2 T_k^{9/2}\left(\frac{15}{8}(x_1+x_2)+\frac{3}{4}(x_1^3+x_2^3)+\frac{1}{2}(x_1^5+x_2^5)+(x_1^7+x_2^7)+x_1^8 Z(x_1)+x_2^8 Z(x_2)\right)\right)\right], \quad (49)$$

$$\delta P_{\parallel_k} = \frac{2n_k}{T_k^{3/2}} \frac{B_0 r}{q} \xi_\perp^r \int_0^{1/B} \mathrm{d}\lambda B\sqrt{1-\lambda B} \left(\frac{2-\lambda B}{BR^2 q}\right) \times \left[\left(\frac{-4}{\tilde{\omega}_d^\varphi}\right)\left(\frac{1}{x_1+x_2}\right)\left(\omega_1 T_k^{7/2}\left(\frac{3}{4}(x_1+x_2)+\frac{1}{2}(x_1^3+x_2^3)+(x_1^5+x_2^5)+x_1^6 Z(x_1)+x_2^6 Z(x_2)\right)\right.\right. \left.\left. + \omega_2 T_k^{9/2}\left(\frac{15}{8}(x_1+x_2)+\frac{3}{4}(x_1^3+x_2^3)+\frac{1}{2}(x_1^5+x_2^5)+(x_1^7+x_2^7)+x_1^8 Z(x_1)+x_2^8 Z(x_2)\right)\right)\right], \quad (50)$$

where we introduced $\omega_1 = -\frac{\omega}{T_k} - \frac{n}{q_k}\left(\frac{1}{n_k}\frac{\partial n_k}{\partial \psi} - \frac{3}{2T_k}\frac{\partial T_k}{\partial \psi}\right)$, $\omega_2 = -\frac{n}{q_k T_k^2}\frac{\partial T_k}{\partial \psi}$, $x_{1,2} = \frac{\tau\sqrt{Q} \pm \tilde{\theta}/\tilde{\omega}_d^\varphi}{2}$, $Q = \left(\frac{\tilde{\theta}}{\tilde{\omega}_d^\varphi}\right)^2 + 4\frac{\omega}{\tilde{\omega}_d^\varphi}$, $\tau = \mathrm{sign}(\tilde{\omega}_d^\varphi)$, $\tilde{\omega}_d^\varphi = -n\omega_d^\varphi T_k/\mathcal{E}$, $\tilde{\theta} = -n\Delta q \dot{\theta}_0 \sqrt{T_k/\mathcal{E}}$. The result is expressed in terms of $Z(x) = \sqrt{\pi} e^{-x^2} i(1 + \mathrm{Erf}(ix))$, the Fried–Conte dispersion function (Fried and Conte 1961). One notes that the parallel and perpendicular perturbed pressures are different, which confirms that unlike the MHD contribution, the kinetic effects we consider are anisotropic.

The integral on the pitch angle can in general not be done analytically, we do it numerically using the trapezoidal rule. Note that these expressions can diverge around $\lambda = 1/B$ as well as when $x_{1,2} \to \infty$. In those cases, we compute the corresponding analytical limit and use it instead of the numerical result in the neighbourhood of the divergence. We use equations (49) and (50) to benchmark `VENUS-KMHD` using the numerical result for ω and $\xi_\perp^r$ in the equations. The result, for the same resonant and non-resonant case as before, is shown in figure 3. The agreement is very good but slight discrepancies are nevertheless observed for both $\delta P_{\perp_k}$ and $\delta P_{\parallel_k}$. The drift-kinetic equation solved by the code (21) differs from the drift-kinetic equation considered in this section (45) because the drifts are slightly approximated in the latter. The approximation is valid if $\Delta q \ll 1$ in the region where the mode is developed. The observed differences are therefore likely the consequence of this assumption. One furthermore notes that the largest differences are observed in the inner region, where q is lower than one, which seems to confirm this hypothesis.

4.2.3. Exact analytical result in a specific limit

We finish this section presenting benchmarks of the kinetic perturbed pressures by noting that it is possible, under certain assumptions, to obtain fully analytical results for $\delta P_{\perp_k}$ and $\delta P_{\parallel_k}$ which, unlike equations (49) and (50) do not require a numerical integration on one of the velocity variable.

The necessary assumptions are the following: in the guiding-centre velocity appearing in the left-hand side of equation (21), only the $v_\parallel$ advection term is considered, the contributions coming from the ∇B and the curvature drifts are dropped (see equation (9)). However, the full expression of $\boldsymbol{v}_{g_k}$ is kept in the right-hand side of the equation. Nevertheless, the effect of the perturbed parallel magnetic field $\delta B_\parallel$ on the drift-kinetic equation is neglected here (the drift-kinetic equation has in this respect an approximation for the perturbed Lagrangian).

This approximation is motivated by the fact that it allows us to obtain fully analytical expressions for the kinetic perturbed pressures as a function of radius if $v_\parallel$ and μ are used as the velocity variables also for the analytical derivation. No further approximation and no numerical resolution or integration is necessary. Moreover, the approximation on $\boldsymbol{v}_{g_k}$ as well as the fact that $\delta B_\parallel$ is ignored can be made consistently in the code and in the analytical derivation. The simplified drift-kinetic equation thus reads:

$$\left(-i\omega + v_\parallel \boldsymbol{b}\cdot\nabla\right)\delta h_k = -i\left(q_k\left(\boldsymbol{\xi}_\perp \times \boldsymbol{B}\right)\cdot\boldsymbol{v}_{g_k}\right)\left(\omega\frac{\partial F_k}{\partial \mathcal{E}} + n\frac{\partial F_k}{\partial P_\varphi}\right). \tag{51}$$

Using equations (25) and (26) and using the fact that we are in cylindrical geometry, equation (51) can be solved to find the equivalent of (42) under the assumptions mentioned above:

$$\delta h_k\left(s, m, n, v_\parallel, \mu\right) = \frac{\xi^r_\perp}{B}\frac{C_{4,0}v_\parallel^4 + \left(C_{2,0} + \mu C_{2,1}\right)v_\parallel^2 + \mu C_{0,1} + \mu^2 C_{0,2}}{\omega - v_\parallel\left(\frac{Fm}{BqR_0^2} + \frac{Fn}{BR_0^2}\right)}F_k, \tag{52}$$

where $C_{4,0} = \frac{nF'^2 r m_k^2}{2Bq^2R_0^4 q_k T_k^2}\frac{\mathrm{d}T_k}{\mathrm{d}\psi}$, $C_{2,0} = \frac{rF'^2 m_k}{Bq^2R_0^4}\left(-\frac{\omega}{T_k} + \frac{n}{q_k n_k}\frac{\mathrm{d}n_k}{\mathrm{d}\psi} - \frac{3n}{2q_k T_k}\frac{\mathrm{d}T_k}{\mathrm{d}\psi}\right)$, $C_{0,2} = -\frac{nB}{2q_k T_k^2}\frac{\mathrm{d}(B^2)}{\mathrm{d}r}\frac{\mathrm{d}T_k}{\mathrm{d}\psi}$, $C_{2,1} = \frac{nm_k}{2q_k T_k^2}\frac{\mathrm{d}T_k}{\mathrm{d}\psi}\left(\frac{2rF'^2}{q^2R_0^4} - \frac{1}{2}\frac{\mathrm{d}(B^2)}{\mathrm{d}r}\right)$ and

$C_{0,1} = \frac{1}{2}\frac{\mathrm{d}(B^2)}{\mathrm{d}r}\left(\frac{\omega}{T_k} - \frac{n}{q_k n_k}\frac{\mathrm{d}n_k}{\mathrm{d}\psi} + \frac{3n}{2q_k T_k}\frac{\mathrm{d}T_k}{\mathrm{d}\psi}\right)$ and F_k is given by (25). Inserting (52) in equations (17) and evaluating the two integrals analytically, one obtains the two kinetic perturbed pressures:

$$\begin{aligned}\delta P_{\perp_k}(s) = &-\frac{\xi^r_\perp B\sqrt{T_k}x}{\omega}\sqrt{\frac{m_k}{2}}\left[C_{4,0}\left(\frac{2T_k^2}{Bm_k}\right)^2\left(\frac{x}{2} + x^3 + x^4 Z(x)\right)\right.\\ &+\left(C_{2,0} + \frac{2T_k}{B}C_{2,1}\right)\left(\frac{2T_k^3}{B^2 m_k}\right)\left(x + x^2 Z(x)\right) + \left(C_{0,1} + \frac{3T_k}{B}C_{0,2}\right)\left(\frac{2T_k^3}{B^3}\right)Z(x)\Big],\end{aligned} \tag{53}$$

$$\begin{aligned}\delta P_{\parallel_k}(s) = &-\frac{\xi^r_\perp B\sqrt{T_k}m_k x}{\omega}\sqrt{\frac{m_k}{2}}\left[\frac{C_{4,0}T_k}{B}\left(\frac{2T_k}{m_k}\right)^3\left(\frac{3x}{4} + \frac{x^3}{2} + x^5 + x^6 Z(x)\right)\right.\\ &+\left(C_{2,0} + \frac{T_k}{B}C_{2,1}\right)\left(\frac{4T_k^3}{Bm_k^2}\right)\left(\frac{x}{2} + x^3 + x^4 Z(x)\right)\\ &+\left.\left(C_{0,1} + \frac{3T_k}{B}C_{0,2}\right)\left(\frac{2T_k^3}{B^2 m_k}\right)\left(x + x^2 Z(x)\right)\right],\end{aligned} \tag{54}$$

where $x = \omega/\left[\sqrt{\frac{2T_k}{m_k}}\left|\frac{Fm}{qBR_0^2} + \frac{Fn}{BR_0^2}\right|\right]$. Now, for a known ω and $\xi^r_\perp$ (obtained from `VENUS-KMHD`), this expression can be easily evaluated to obtain the perturbed kinetic pressure, compared with the code results. The plasma dispersion function Z is evaluated using the numerical implementation included in `SciPy`, except around the rational surface ($x \to \infty$) where the numerical implementation fails to give the correct result. Near the rational surface we use instead the analytical limit computed using a series expansion of $Z(x)$, as already done above in the general case.

The comparison of the two kinetic perturbed pressures for a resonant $n = m = 1$ internal kink mode is shown in figure 4. Once again, excellent agreement is observed. The slight discrepancy observed in the parallel perturbed pressure around the rational surface is due to the use, for the analytical result, of the analytical limit for $x \to \infty$ also in the vicinity of the rational surface, where it is no longer exactly correct but the numerical result is still unusable.

4.3. Full benchmark in the low and high frequency limit

In the two following sections, we present a benchmark for the full kinetic-MHD problem. Shown is a semi-analytical approach for the growth rate of a kinetic-MHD mode and associated benchmarks for the growth rate obtained from `VENUS-KMHD`. This will be undertaken in two opposite limits, the low frequency and the high frequency limits. Each allows us to test only part of the implementation of the drift-kinetic equation, but because we consider the two opposite cases, almost all the terms in

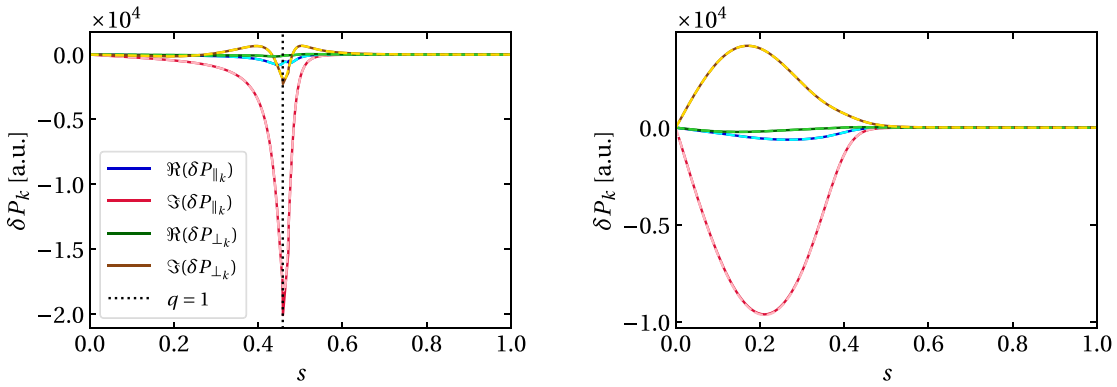


Figure 4. Comparison of the kinetic perturbed pressures $\delta P_{\perp_k}, \delta P_{\parallel_k}$ obtained with `VENUS-KMHD` (dashed lines) and using the fully analytical relations (53) and (54) (solid lines). In each case, the real and imaginary parts are shown. The MHD displacement and the growth rate used in the analytical relations are taken from the numerical result. A resonant-case (*left*) and a non-resonant case (*right*) are shown. For the former, the rational surface $q = 1$ associated with the considered $n = m = 1$ internal kink mode is shown by the vertical dotted line. The additional assumptions required to obtain a fully analytical solution were consistently applied in the code, to allow for a fair comparison.

the full equations are tested at least by one of the limits. Because the analytical treatment described below is most accurate at low pressure, we consider in this section an internal kink mode with $\beta_{\text{tot}}(0) = \mu_0 P(0)/B_0^2 = 0.11\%$ and $\beta_{\text{kin}}(0)/\beta_{\text{tot}}(0) = 0.53$ on the axis, where we define $\beta_{\text{kin}}(0) = \mu_0 P_k(0)/B_0^2$. The resonant safety factor profile is still given by (27) with the usual parameters. The non-resonant $q-$profile is given by (28), with $q_0 = 1.001$. Since the pressure is smaller than in our reference case, it is necessary to bring q_0 closer to 1 to ensure the mode will still be unstable. Note that the derivation of the governing equations requires a number of assumptions which will be detailed below. These approximations are not done consistently in the `VENUS-KMHD` results with the exception of approximation (41) for $\delta B_\parallel$. We typically present one result using the exact expression for $\delta B_\parallel$ and one result using the approximation, the latter being expected to match better with the governing equations results.

4.3.1. Low frequency limit

First, we consider the low frequency limit, that is we assume $\omega \ll \omega_d^\varphi, \omega_*$ and $\Delta q \dot{\theta}_0 \ll \omega_d^\varphi$. When comparing the results with `VENUS-KMHD` later, we will artificially remove in the code the corresponding terms: in the numerator, the $\partial F_k/\partial \mathcal{E}$ term is neglected and in the denominator, we keep only $\boldsymbol{v}_{\boldsymbol{d}_k} \cdot \boldsymbol{\nabla}$ (see also equation (9)). In this limit, the solution of equation (45) is:

$$\delta h_k = \frac{\omega_{d0}^\varphi \xi_\perp^r}{\omega_d^\varphi} \frac{\partial F_k}{\partial r}. \tag{55}$$

We now follow Graves *et al* (2021) to obtain a governing equation for the kinetic-MHD problem in the low frequency limit. For this purpose, we define the radial and the toroidal vorticity operators:

$$V_r(\mathbf{X}) = \frac{1}{2\pi} \int_{-\pi}^{\pi} \mathrm{d}\theta \frac{e^{im\theta}}{im} J \boldsymbol{\nabla} \cdot \left(\frac{\mathbf{X} \times \boldsymbol{\nabla} r}{\mathbf{B} \cdot \boldsymbol{\nabla} \varphi} \right), \tag{56}$$

$$V_\varphi(\mathbf{X}) = \frac{1}{2\pi} \int_{-\pi}^{\pi} \mathrm{d}\theta \frac{e^{im\theta}}{im} \frac{R_0 J}{B_0} \boldsymbol{\nabla} \cdot \left(\frac{\mathbf{X} \times \boldsymbol{\nabla} \varphi}{\mathbf{B} \cdot \boldsymbol{\nabla} \varphi} \right), \tag{57}$$

where $\boldsymbol{X}$ is the vector on which we apply the vorticity operator, B_0 is the equilibrium magnetic field at the magnetic axis and J is the Jacobian of the coordinate system. Following the work of Graves *et al* (2021), we do an expansion in large aspect ratio, that is small inverse aspect ratio $\epsilon = r/R_0$. In a cylinder, a large aspect ratio corresponds to a case where the poloidal magnetic field is significantly smaller than the field parallel to the axis of the cylinder, $B_\theta/B_\varphi = \epsilon^2/q$. We use the following definition for the MHD displacement variable: $\boldsymbol{\xi}_\perp = \boldsymbol{\xi}_{\boldsymbol{B}}$, where $\boldsymbol{\xi}_{\boldsymbol{B}} \cdot \boldsymbol{\nabla} \varphi = 0$, $\xi_\perp^r = (F/F_0) \boldsymbol{\xi}_{\boldsymbol{B}} \cdot \boldsymbol{\nabla} r$ and $\xi_\perp^\theta = (F/F_0) \boldsymbol{\xi}_{\boldsymbol{B}} \cdot \boldsymbol{\nabla} \theta$, where $F_0 = R_0 B_0$. This slightly differs from the definition used in Graves *et al* (2021), but remains very similar. We first impose $V_r(\tilde{\boldsymbol{X}}) = 0$, where $\tilde{\boldsymbol{X}}$ is the MHD momentum equation without the inertia term and kinetic perturbed pressures. From this, we obtain the following relation up to order 2 in ϵ which

gives us the poloidal displacement as a function of the radial displacement:

$$\xi_\perp^\theta = \frac{i}{r}\left[\frac{\xi_\perp^r + r\frac{\mathrm{d}\xi_\perp^r}{\mathrm{d}r}}{m} + \frac{\epsilon\alpha\xi_\perp^r}{2mq^2} - \epsilon^2\frac{2m^2q\xi_\perp^r - m^2r\xi_\perp^r\frac{\mathrm{d}q}{\mathrm{d}r} - mnq^2\left(\xi_\perp^r - r\frac{\mathrm{d}\xi_\perp^r}{\mathrm{d}r}\right) + n^2q^3\left(\xi_\perp^r + r\frac{\mathrm{d}\xi_\perp^r}{\mathrm{d}r}\right)}{m^3q^3}\right]. \tag{58}$$

This corresponds to equations (1988) and (33) of Graves *et al* (2021). The differences are due to the slightly modified definition of the components of $\boldsymbol{\xi}_\perp$ as well as to the different convention for the sign of the toroidal mode number n. Note that in principle, one should include the kinetic pressures when computing the radial vorticity. This would result in additional terms in (58) proportional to the kinetic pressures. In order to simplify the computation, we drop those corrections and assume that the kinetic pressure and the total pressure are sufficiently small to make those terms negligible, which justifies this approximation.

We then insert this relation in the MHD equation. The equation $V_\varphi(\boldsymbol{X}) = 0$, where $\boldsymbol{X}$ is the full kinetic-MHD momentum equation (now including kinetic effects), gives a *governing equation*. It is an eigenvalue equation whose eigenvalue is the growth rate $\gamma = \Im(\omega)$ and eigenvector is the radial MHD displacement $\xi_\perp^r$. One can expect that our governing equation will contain terms associated with the ideal MHD response as well as one or several kinetic corrections that encapsulate the kinetic effects. We do not detail the derivation of the governing equation for the standard ideal MHD (see Graves *et al* (2021)). The result is:

$$\frac{1}{r}\frac{\mathrm{d}}{\mathrm{d}r}\left[\left(\left(\frac{\gamma}{\omega_\mathrm{A}}\right)^2 + f^2\right)r^3\frac{\mathrm{d}\xi_\perp^r}{\mathrm{d}r}\right] - \left(m^2-1\right)\left(\left(\frac{\gamma}{\omega_\mathrm{A}}\right)^2 + f^2\right)\xi_\perp^r + \frac{\epsilon^2}{q_s^2}\left(\frac{3}{q_s} + \frac{1}{q(r)}\right)\left(\frac{1}{q(r)} - \frac{1}{q_s}\right)\xi_\perp^r + \frac{\epsilon\alpha}{q_s^4}\xi_\perp^r + X_\mathrm{kin} = 0, \tag{59}$$

where $f = 1/q - 1/q_s$, $q_s = q(s_\mathrm{res}) = -m/n$, s_res is the location of the rational surface, $\alpha = -\frac{2\mu_0q^2R_0}{B_0^2}\frac{\mathrm{d}P}{\mathrm{d}r}$, $\epsilon = r/R_0$, ω_A is the Alfvén frequency and X_kin is the kinetic correction that will be detailed below. Note that the analytical solution (19) of (3) was used to express all occurrences of $\mathrm{d}F/\mathrm{d}r$ as a function of derivatives of the total pressure, that is in terms of α. The remaining occurrences of F were replaced by R_0B_0 and terms involving the magnetic shear were neglected.

In order to obtain the kinetic part of the governing equation, we need to compute the toroidal vorticity of the terms involving the perturbed kinetic pressures. Adopting the vorticity operator on the kinetic pressure tensor, following a similar approach to the construction of quadratic forms, where the kinetic contributions to δW can be written in terms of a velocity integral with integrand being the product of δh_k and the toroidal drift precession (Antonsen and Lee 1982), it can be shown that in a cylinder one obtains exactly (Graves 2020):

$$V_\varphi\left(\underbrace{\left(\delta P_{\perp_k} - \delta P_{\parallel_k}\right)\boldsymbol{\kappa} - \boldsymbol{\nabla}_\perp\delta P_{\perp_k}}_{\boldsymbol{X}_\mathrm{kin}}\right) = m_k\frac{R_0}{B_0}\int \mathrm{d}v^3\,\frac{J}{q}\frac{\Omega_{c_k}\omega_d^\varphi}{B}\delta h_k. \tag{60}$$

This result is obtained in a cylinder because there is no radial drift motion, so that geodesic curvature, and hence associated inertial enhancement (Graves *et al* 2000), can be neglected.

In the above, $\Omega_{c_k} = q_kB/m_k$ is the cyclotron frequency for the kinetic species k. Using the solution for the drift-kinetic equation in the low frequency limit (55), we have:

$$V_\varphi\left(\boldsymbol{X}_\mathbf{kin}\right) = \frac{m_k}{B_0}\int \mathrm{d}v^3\,\frac{r}{B}\frac{1}{q^2}\left(v_\parallel^2 + \frac{\mu B}{m_k}\right)\xi_\perp^r\frac{\partial F_k}{\partial r}, \tag{61}$$

where we used $J = rR_0$ in a cylinder as well as equation (44). We have:

$$V_\varphi\left(\boldsymbol{X}_\mathbf{kin}\right) = \frac{r\xi_\perp^r}{BB_0q^2}\left(\underbrace{\int \mathrm{d}v^3\,m_kv_\parallel^2\frac{\partial F_k}{\partial r}}_{\frac{\mathrm{d}P_{k_\parallel}}{\mathrm{d}r}} + \underbrace{\int \mathrm{d}v^3\,\mu B\frac{\partial F_k}{\partial r}}_{\frac{\mathrm{d}P_{k_\perp}}{\mathrm{d}r}}\right), \tag{62}$$

where we identified the radial derivatives of the equilibrium pressures. Since our equilibrium state is isotropic, we have $P_{\perp_k} = P_{\parallel_k} = P_k$ where $P_k = n_k T_k$ is the equilibrium pressure associated with the kinetic species. Therefore:

$$V_\varphi(\boldsymbol{X}_{\mathbf{kin}}) \cong -2\frac{r\xi_\perp^r}{BB_0q^2}\frac{\mathrm{d}P_k}{\mathrm{d}r} = -\frac{B_0}{B}\frac{\epsilon\alpha_{\mathrm{kin}}}{q^4}\xi_\perp^r = X_{\mathrm{kin}}, \tag{63}$$

where $\alpha_{\mathrm{kin}} = -2\mu_0 R_0 q^2(\mathrm{d}P_k/\mathrm{d}r)/B_0^2$ is the pressure parameter corresponding to the equilibrium pressure of the kinetic species. We note that at the lowest order in ϵ, that is if $B_0/B \approx 1$, the kinetic effect exactly cancels the contribution of the kinetic species to the (Suydam) interchange term $\epsilon\alpha/q^4$. More precisely, the last term in (59) cancels with the contribution of the kinetic particles to the second to last term in the same equation. Since the interchange term is destabilising for the internal kink mode in a cylinder, it means that the low frequency kinetic effect is stabilising. This kinetic effect is analogous to the low-frequency result in a torus, where the kinetic effect cancels the destabilising contribution of trapped ions to the ideal fluid response, leaving the stabilising fluid effect of passing ions (see e.g. appendix of Graves *et al* (2003)).

We can now use the governing equation formed by (59) and (63) as a benchmark for the `VENUS-KMHD` code. We solve the governing equation numerically using `VENUS-MHD`, since it can be written as a generalised eigenvalue problem for the eigenvalue γ and corresponding eigenvector $\xi_\perp^r$. Note that even if we solve the governing equation with `VENUS-MHD`, this is still a meaningful benchmark because the governing equation is an equation for only one component of the displacement $\boldsymbol{\xi}_\perp$ and the kinetic effects were solved completely analytically. In `VENUS-KMHD`, the low frequency limit is achieved by removing from the matrices the terms that are neglected in the drift-kinetic equation. Note that this would make the matrix B singular, which is not handled by our eigenvalue solver. To avoid this issue, instead of completely removing the terms from the equations, we put a flag equal to 10^{-7} in front of the terms that should be neglected. It was verified that this value of the flag is appropriate to converge to the low frequency limit. It is because of these numerical difficulties that the Krylov–Schur eigenvalue solver with LU shift-invert was used for these results instead of the usual generalised Davidson eigenvalue solver.

The result of the benchmark is shown in figure 5 for both the resonant and non-resonant safety factor profile: In both cases, we show a scan on the kinetic fraction $\beta_{\mathrm{kin}}(0)/\beta_{\mathrm{tot}}(0)$ at constant total pressure ($\beta_{\mathrm{tot}}(0) = 0.11\%$) as well as a scan on the total pressure at constant kinetic fraction ($\beta_{\mathrm{kin}}(0)/\beta_{\mathrm{tot}}(0) = 0.53$). The first scan corresponds to a case where our hot minority ions are divided into two subspecies with equal physical parameters, one that is treated kinetically and the other one that is considered as a fluid species (so it is only entering in the ideal MHD equation). By varying the fraction of those two subspecies, one evolves from a case that matches the ideal MHD result to the case where the hot particles are fully kinetic. We do this while keeping the total pressure constant. The main advantage of this approach is that the ideal growth rate, which depends on the total pressure gradient, stays constant throughout the scan. As a consequence, the observed variation of the growth rate is purely due to the kinetic effects.

Note that because the governing equation is not exactly equivalent to the true MHD momentum equation, the ideal growth rate obtained when solving the ideal governing equation will not exactly match the ideal growth rate obtained when solving the ideal MHD momentum equation with `VENUS-MHD`. Because we are interested in the kinetic effect, that is the deviation of the ideal result due to kinetic effects, we show in figure 5 the difference between the kinetic-MHD growth rate $\gamma_{\text{kinetic-MHD}}$ and the ideal growth rate γ_{MHD}:

$$\Delta\gamma_{\mathrm{kin}} = \gamma_{\text{kinetic-MHD}} - \gamma_{\text{ideal MHD}}. \tag{64}$$

The objective is to identify the true kinetic contribution to the growth rate. In this way, we do not get distracted by discrepancies in the ideal growth rate and can focus on the comparison of the kinetic correction obtained with the governing equation and with `VENUS-KMHD`.

The fact that $\gamma_{\text{kinetic-MHD}} - \gamma_{\text{ideal MHD}}$ is negative indicates that the kinetic effects are stabilising, as predicted above, because they cancel the contribution of the hot particles in the destabilising interchange term. One observes good agreement of the governing equation results with the fully numerical results obtained with `VENUS-KMHD`. A more significant discrepancy is observed at higher total pressure. The more erratic behaviour of the `VENUS-KMHD` results can be explained by the increasing difficulty with increasing β to converge to the low-frequency limit. As noted before, it can only be approached since it is numerically singular. Moreover, this discrepancy can also be explained by the fact that the terms we

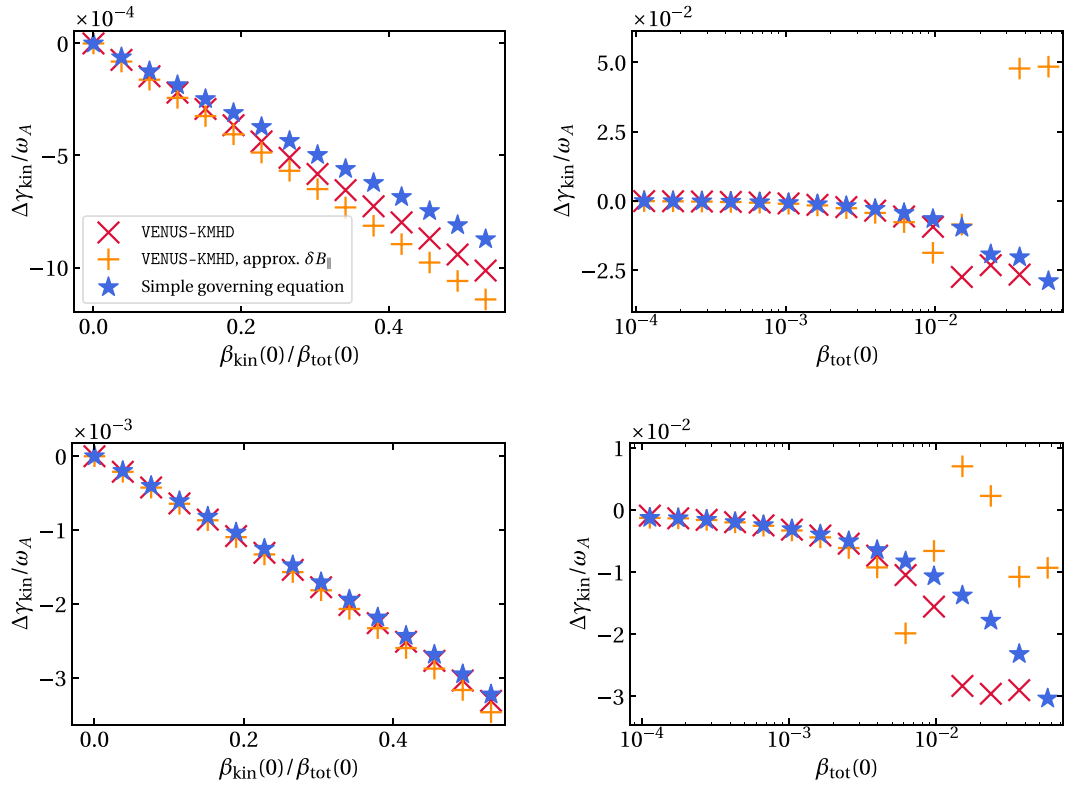


Figure 5. Kinetic correction on the growth rate in a scan on the fraction of kinetic particles at constant total pressure (*left column*) and a scan on the total pressure at constant kinetic fraction (*right column*) in the low-frequency limit. This shows a resonant case (*top row*) and a non-resonant case (*bottom row*). The results obtained with `VENUS-KMHD` are shown using either the exact expression (red) or the approximation (41) for $\delta B_\parallel$ (orange) which was also used when obtaining the governing equation.

neglected in our analytical computation are proportional to the pressure (both total and kinetic pressure) and they start to become important at higher β. In order to have a good match at higher pressure, it would be necessary to include the kinetic effects in equation (58) and recompute the toroidal vorticity and the resulting governing equation accordingly. Moreover, the ordering in inverse aspect ratio (large B_φ/B_θ) used to derive the governing equation starts to break down at large total pressure. This also the case of our simple approximation for $\delta B_\parallel$. From equation (55), one can estimate the kinetic perturbed pressures as $\delta P_{\perp,\parallel_k} \sim \xi^r_\perp \mathrm{d}P_k/\mathrm{d}r$. This indicates that the approximation (41) for $\delta B_\parallel$ should be valid in the low frequency limit as long as $\mathrm{d}P_k/\mathrm{d}r \ll \mathrm{d}P/\mathrm{d}r$. This is no longer true at the largest values of $\beta_{\rm tot}$ considered in the right column of figure 5.

4.3.2. High frequency limit

We now consider the limit $\omega \gg \omega_d^\varphi, \omega_*, \Delta q\dot{\theta}_0$ (Kruskal and Oberman 1958). Similarly to what was done in the low frequency case, when comparing the results with `VENUS-KMHD` later, we will artificially remove the matrix elements associated with the drift-kinetic equation that do not contain ω. For this computation, we go back to the notation of section 4.1, which is more convenient in this case since one wants to avoid doing any approximation, and we use $v_\parallel, \mu$ as velocity variables. Equation (42) reduces in this limit to:

$$\delta h_k = -\left[\frac{\xi^r_\perp rF}{qR_0^2B^2}\left(\frac{m_k v_\parallel^2 F}{qR_0^2} - \mu B\left(\frac{\mathrm{d}}{\mathrm{d}r}\left(\frac{rB}{qR_0^2}\right) + \frac{1}{R_0}\frac{\mathrm{d}F}{\mathrm{d}r}\right)\right) - \mu\delta B_\parallel\right]\frac{F_k}{T_k}, \tag{65}$$

where the explicit expression of $\frac{\partial F_k}{\partial \mathcal{E}}$ was replaced using (25). Using equations (17) and (41), one computes the kinetic perturbed pressures:

$$\delta P_{\perp_k} = \xi^r_\perp P_k\left[\frac{1}{B^2}\frac{\mathrm{d}\left(B^2\right)}{\mathrm{d}r} + \frac{2\mu_0}{B^2}\frac{\mathrm{d}P}{\mathrm{d}r} - \frac{rF^2}{q^2R_0^4}\right], \tag{66}$$

$$\delta P_{\|_k} = \xi_\perp^r P_k \left[\frac{1}{2B^2} \frac{\mathrm{d}\left(B^2\right)}{\mathrm{d}r} + \frac{\mu_0}{B^2} \frac{\mathrm{d}P}{\mathrm{d}r} - \frac{3rF^2}{q^2 R_0^4} \right]. \tag{67}$$

Using equations (22), (66) and (67), one can compute the kinetic pressure terms in (20) exactly. We start by reproducing the approach followed in section 4.3.1 for the low-frequency limit. The result of the radial vorticity gives once again (58). Replacing this in the MHD momentum equation gives once again (59). In the case of the high frequency limit, the kinetic correction is:

$$X_{\mathrm{kin}} = \frac{\epsilon^2 \mu_0 P_k \xi_\perp^r}{B_0^2 q^4} \left(2m^2 + 9mnq\right) + \frac{3\mu_0 m^2 \epsilon \alpha P_k \xi_\perp^r}{2B_0^2 q^4} + \frac{3\mu_0 \epsilon^2 r P_k \frac{\mathrm{d}\xi_\perp^r}{\mathrm{d}r}}{q^4} m\left(m + nq\right). \tag{68}$$

One notices that all these terms are smaller than the kinetic effect in the low frequency limit, which was given by equation (63) by a factor $\mu_0 P_k / B_0^2$. As a consequence, one can expect the kinetic corrections to be weaker in this limit compared to the low frequency limit. The first term of (68) corresponds to a stabilising effect while the two others are destabilising.

Because the kinetic effect in this limit is smaller than it was in the low frequency limit, we decide to also consider here the indirect kinetic effects that enter through the relation giving $\xi_\perp^\theta$ as a function of $\xi_\perp^r$. These effects are indirect in the sense that the kinetic effects appearing in $\xi_\perp^\theta$ will affect the final result only through the ideal part of the MHD momentum equation. This is because, as mentioned above, in cylindrical geometry, kinetic pressure terms depend only on $\xi_\perp^r$. This can be verified by inspection of (66) and (67) and is a consequence of the lack of radial drifts in cylindrical geometry.

In order to obtain the kinetic correction to the poloidal displacement, we need to calculate once again the radial vorticity. Writing (20) as $\boldsymbol{X_I} = \boldsymbol{X_W}$, we enforce:

$$V_r\left(\boldsymbol{X_W}\right) = 0, \tag{69}$$

where the V_r operator is defined in equation (56). Similarly to what we did in the low frequency limit, the inertia is ignored in the radial vorticity, but this time, the kinetic effects are included. We solve (69) for the poloidal displacement and obtain, up to order 2 in ϵ:

$$\xi_\perp^\theta = \frac{i}{r} \left[\frac{\xi_\perp^r + r\frac{\mathrm{d}\xi_\perp^r}{\mathrm{d}r}}{m} + \frac{\epsilon\alpha\xi_\perp^r}{2mq^2} + \frac{3\mu_0\epsilon^2 P_k \xi_\perp^r}{mq^2 B_0^2} \right.$$
$$\left. -\epsilon^2 \frac{2m^2 q\xi_\perp^r - m^2 r\xi_\perp^r \frac{\mathrm{d}q}{\mathrm{d}r} - mnq^2\left(\xi_\perp^r - r\frac{\mathrm{d}\xi_\perp^r}{\mathrm{d}r}\right) + n^2 q^3\left(\xi_\perp^r + r\frac{\mathrm{d}\xi_\perp^r}{\mathrm{d}r}\right)}{m^3 q^3} \right]. \tag{70}$$

Note that this is equal to (58) except for the last term of the first line that is a kinetic correction to the ideal variable $\xi_\perp^\theta$. We replace $\xi_\perp^\theta$ by (70) in (20) to obtain the final governing equation. As in the previous section, we also assume that q is close to 1 where the mode is developed, that is $q + m/n$ is small. With these assumptions, we once again compute $V_\varphi(\boldsymbol{X}) = V_\varphi(\boldsymbol{X_I} - \boldsymbol{X_W})$ (see definition of V_φ in (57)) and obtain (59). Only the kinetic correction differs. The modification due to the indirect kinetic effect entering through $\xi_\perp^\theta$ is also absorbed into the new expression for X_{kin}, which is now given by:

$$X_{\mathrm{kin}} = \frac{\epsilon^2 \mu_0 P_k \xi_\perp^r}{B_0^2 q^4} \left(8m^2 + 24mnq + 9n^2 q^2\right) + \frac{3\mu_0 \epsilon^2 r P_k \frac{\mathrm{d}\xi_\perp^r}{\mathrm{d}r}}{q^4} \left(m + nq\right)^2. \tag{71}$$

As already discussed before, not all the kinetic effects come from $V_\varphi((\delta P_{\perp_k} - \delta P_{\|_k})\boldsymbol{\kappa} - \boldsymbol{\nabla}_\perp \delta P_{\perp_k})$, which means that $V_\varphi(\boldsymbol{X_{\mathrm{kin}}}) \neq X_{\mathrm{kin}}$. Some come from the toroidal vorticity of the ideal MHD equation, because $\xi_\perp^\theta$ is altered by the kinetic effects, which is also in X_{kin} above. Comparing equations (68) and (71) indicates the approximation associated with neglecting the kinetic correction in (70). One recognises the first and third terms of (68) in (71) with slightly different coefficients. But most importantly, the second term of (68) is totally absent from our updated computation, a cancellation happens between the kinetic effects coming directly from the toroidal vorticity of $\boldsymbol{X_{\mathrm{kin}}}$ and those entering through $\xi_\perp^\theta$. Since the last term of the kinetic correction is proportional to $(m + nq)$, which is small where the internal kink mode is located (recall that we use a negative n and positive m, q), one can predict that the first term is going to dominate the high-frequency kinetic response, which will be stabilising. In the limit $q = -m/n$ one obtains

$$X_{\mathrm{kin}} \approx -7m^2 \frac{\epsilon^2 \mu_0 P_k \xi_\perp^r}{B_0^2 q^4}. \tag{72}$$

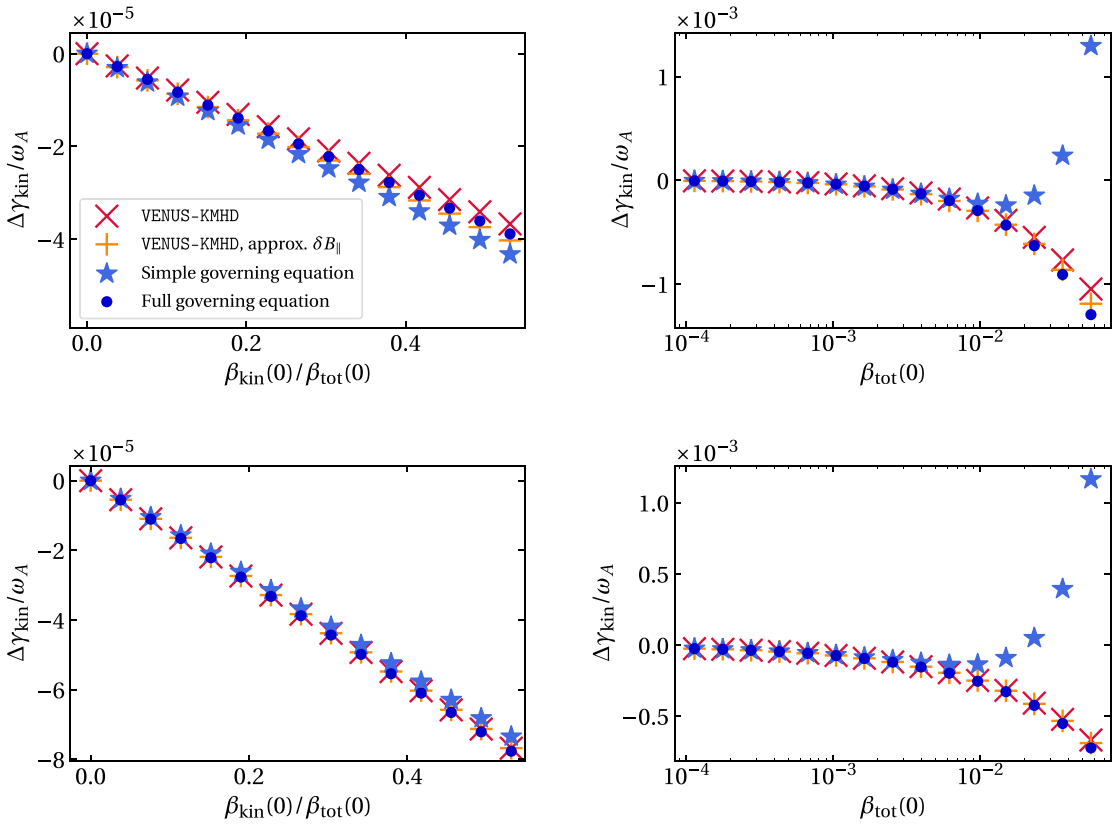


Figure 6. Kinetic correction on the growth rate in a scan on the fraction of kinetic particles at constant total pressure (*left column*) and a scan on the total pressure at constant kinetic fraction (*right column*) in the large-frequency limit. This shows a resonant case (*top row*) and a non-resonant case (*bottom row*). The results obtained with `VENUS-KMHD` are shown using either the exact expression (red) or the approximation (41) (orange), used also in the analytical work leading to the governing equation for $\delta B_\parallel$. Two different governing equations are compared, one (light blue), ignoring kinetic effects when using the radial vorticity to link the poloidal displacement to the radial one, as done in section 4.3.1, the other (dark blue) including this effect.

At this stage, one can solve numerically the governing equation formed by equations (59) and (71) for $\xi^r_\perp$ and ω and compare with the `VENUS-KMHD` result. Similarly to what was done in section 4.3.1 for the low-frequency limit, we study the behaviour as a function of the kinetic fraction at fixed total pressure as well as the behaviour in terms of the total pressure at fixed kinetic fraction, both for a resonant and a non-resonant $q-$profile. The result is shown in figure 6 where one verifies that the kinetic effects in the high frequency limit are stabilising, as predicted. Once again, good agreement is observed between the governing equation and the numerical results. As expected, the plots of the simplified governing equation, which neglect the kinetic corrections in the ideal MHD equation show a bigger discrepancy compared to the code compared to the fully consistent model. The difference is significant at higher kinetic fraction and, most importantly, at higher total pressure, as also observed in section 4.3.1. On the other hand, the consistent analytical model shows excellent agreement up to high values of β. The complete analytical model exhibits particularly good agreement with the `VENUS-KMHD` result when using the same approximation for $\delta B_\parallel$ as the analytical work, as expected. Note that this approximation works well in this limit. From equation (66), one has $\delta P_{\perp_k} \sim \epsilon \xi^r_\perp P_k/R_0$. This means that approximation (41) for $\delta B_\parallel$ is appropriate as long as $\mathrm{d}P/\mathrm{d}r \gg \epsilon P_k/R_0$, which is typically the case in these results.

5. Results in cylindrical geometry

In this section, we present a few results in cylindrical geometry outside of the two limits explored so far. All the physics is now included and the goal of this section is to explore the capabilities of the `VENUS-KMHD` code. Note that from now on, only the exact expression for $\delta B_\parallel$ will be used. In this section, $N_{v_\parallel} = 80$, $N_\mu = 40$ was used. We consider the usual resonant and non-resonant cases. For each

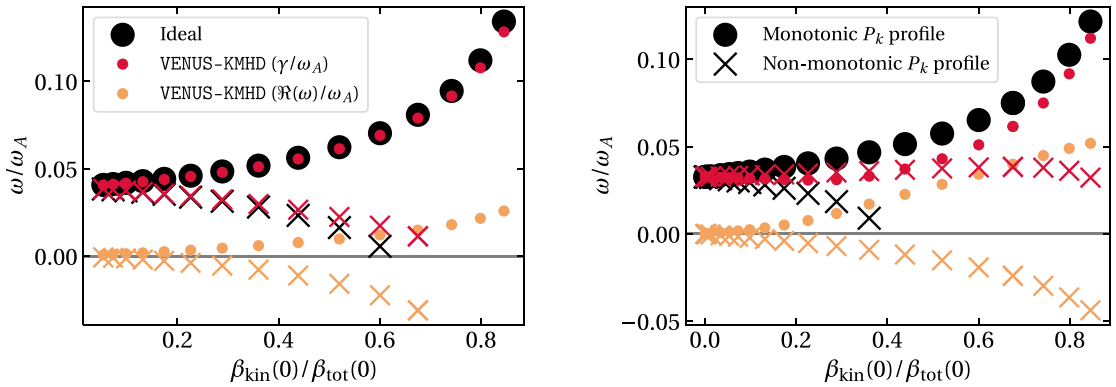


Figure 7. Scan on the hot particles density for a resonant (*left*) and a non-resonant (*right*) case. The sets of points shown are the growth rate of the ideal result from `VENUS-MHD` (black) as well as the growth rate (red) and the real frequency (orange) of the kinetic-MHD results from `VENUS-KMHD`. The circle markers correspond to the case where the hot kinetic particles have the same pressure profile as the main ions and electrons while the crosses correspond to a case where the hot particles kinetic pressure follows a non-monotonic pressure profile that peaks at $s = 0.6$. Note that β on the axis is used for this figure. In the non-monotonic pressure case, it can be smaller than the maximum β. The horizontal grey line indicates $\omega = 0$, which in the case of the growth rate corresponds to a stable mode.

one, two sub-classes are simulated, one where the kinetic hot α particles have the same density and temperature profiles as the main ions and electrons, another one which has an inverse pressure gradient in the inner region. In the latter case, the pressure peaks at $s = 0.6$ and then goes to zero at the edge, as usual. This is achieved using for the number density and for the temperature of the hot kinetic particles profile (27) with $\eta = 6.35$, $\Delta = -1$, $s_{\rm ref} = 0.6$, $\nu = 2$, $\mu = 2$. Here, we consider an ideal MHD case to which we add more and more kinetic hot particles. As a consequence, the total pressure is not constant and the ideal growth rate will also change throughout the scan. Note that in addition to the hot ion contribution, the main electrons will also contribute more and more as their pressure needs to also increase to ensure quasi-neutrality. As a consequence, we must record the ideal and the kinetic-MHD growth rate, the difference between the two giving the kinetic effect. The results are presented in figure 7.

Focusing first on the ideal result, one observes that the addition of hot particles has a destabilising effect when their pressure profile is monotonically decreasing but stabilising when the pressure increases in the inner region. This can easily be understood by remembering that these modes are mostly driven unstable by the pressure gradient in the inner region, where the field-line bending terms are small enough to allow the mode to develop (because the safety factor profile is close to one). In the case where all species have the same pressure profile, adding more and more hot kinetic particles increases the total pressure without changing its shape and therefore makes the pressure gradient stronger, which makes the mode more unstable. On the other hand, if the kinetic particles have a non-monotonic pressure profile, the total pressure gradient in the inner region becomes smaller and smaller as we add more kinetic particles, which decreases the pressure drive and as a consequence the growth rate of the mode.

Now focusing on the kinetic effect, one can observe that in the case with monotonic pressure profile for all species, the kinetic-MHD result follows the trend of the ideal result but with a smaller slope. This means that the kinetic effects in this case are stabilising, the kinetic-MHD result is less unstable than the ideal solution.

The physics at play is more complex and more interesting if the kinetic particles have a non-monotonic pressure profile. In this case, the kinetic effect is destabilising. It is observed that the kinetic-MHD growth rate is everywhere larger than the ideal growth rate. Using an increasing pressure profile in the inner region reverses the sign of $\partial F_k/\partial P_\varphi$, which can be sufficient to change the sign of the total kinetic effect if one is not in the high frequency limit. Beyond a critical amount of kinetic hot particles ($\beta_{\rm kin}(0)/\beta_{\rm tot}(0) \simeq 0.6$ in the resonant case and $\beta_{\rm kin}(0)/\beta_{\rm tot}(0) \simeq 0.4$ in the non-resonant case), the total pressure gradient in the inner region is too weak to drive the ideal mode unstable and it reaches marginal stability. The kinetic-MHD solution however remains unstable until a much larger hot particle pressure is reached. In this region, the kinetic effects alone are sufficient to drive unstable a mode which ideally would be marginally stable. Finally, beyond another critical value of the hot particles pressure, even the kinetic-MHD result with resonant $q-$profile reaches marginal stability beyond $\beta_{\rm kin}(0)/\beta_{\rm tot}(0) \simeq 0.7$ while the non-resonant case remains unstable. When the total pressure becomes

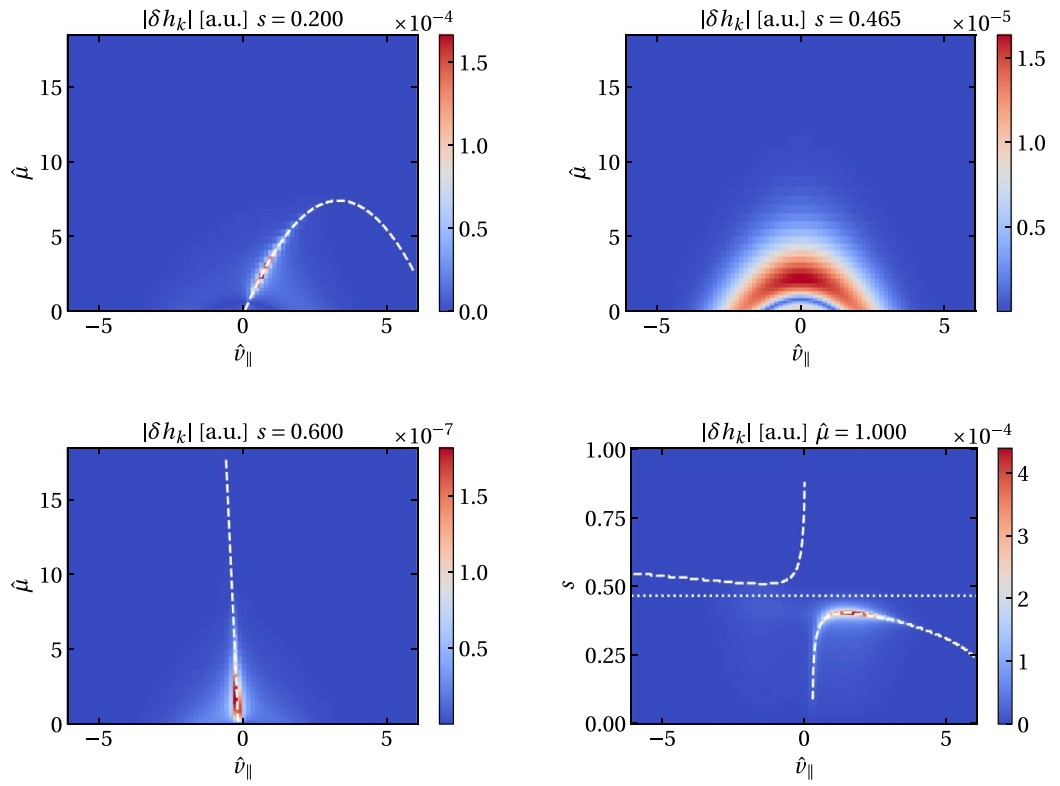


Figure 8. Visualisation of the kinetic perturbed distribution function δh_k in the normalised velocity space $\hat{v}_\parallel, \hat{\mu}$ at three different radial locations and as a function of s and $\hat{v}_\parallel$ for $\hat{\mu} = 1$ (*bottom right*). The situation considered here is a resonant case with non-monotonic hot pressure profile and $\beta_{\text{kin}}(0)/\beta_{\text{tot}}(0) = 0.67$. The radial location shown in the top right plot corresponds to the $q = 1$ rational surface. The dashed white lines indicate the locations where the resonance condition (73) is satisfied. The dotted line indicates the location of the $q = 1$ rational surface. Note that the ranges of the colorbars differ in each subplot.

increasing in the inner region due to the dominant effect of the hot particles, the pressure gradient has a stabilising effect which must be compensated by the kinetic effects. Past a certain threshold, the kinetic effects are insufficient to do so and the mode is fully stabilised.

The real frequency of the mode is also shown in figure 7. As expected, it gets larger with stronger kinetic effects and tends to zero when they become negligible, therefore matching the ideal MHD result which has $\Re(\omega) = 0$. It is interesting to observe that the real frequency of the mode changes sign depending on whether a standard monotonic pressure profile is used for the hot kinetic ions (positive $\Re(\omega)$) or a non-monotonic hot pressure profile is used (negative $\Re(\omega)$). However, for a given pressure profile, the sign is the same with a resonant or a non-resonant safety factor profile. One observes that when the non-monotonic pressure profile is used, the real frequency is often larger (in absolute value) than the growth rate. It is the opposite when the standard pressure profile is considered.

Since the kinetic perturbed distribution function δh_k is part of the eigenvector of our kinetic-MHD problem, it is readily available and one can look at its structure. As an example, this is presented for two of the four results of figure 7: the resonant case with non-monotonic hot particles pressure profile (figure 8) and the non-resonant case with monotonic hot particles pressure profile (figure 9). We show in each case δh_k as a function of the normalised velocity variables $\hat{v}_\parallel, \hat{\mu}$ at three specific radial locations and as a function of s and $\hat{v}_\parallel$ at fixed $\hat{\mu} = 1$. Since a single Fourier mode is sufficient to represent the poloidal direction in a cylinder, we see here the coefficient corresponding to this only mode. In order to emphasize the wave-particle resonant interactions in the kinetic-MHD response, the locations in phase space where the real part of the denominator of (42) cancels, that is where the wave-particle resonant condition is exactly satisfied, are also represented in the figures. The resonance condition is repeated in equation (73).

The $q = m/n$ resonant case shown in figure 8, which exhibits a destabilising effect, shows a strong wave-particle resonance in the inner region. It is observed that the numerical result for δh_k is strongly matching the region of wave-particle resonance, which is caused by the interaction between the real frequency of the kinetic-MHD mode and the average of the guiding frequency $\boldsymbol{v}_{\boldsymbol{g}_k} \cdot \boldsymbol{\nabla}$. At the rational surface, there is no possibility of wave-particle resonance, and we observe a perturbed distribution function

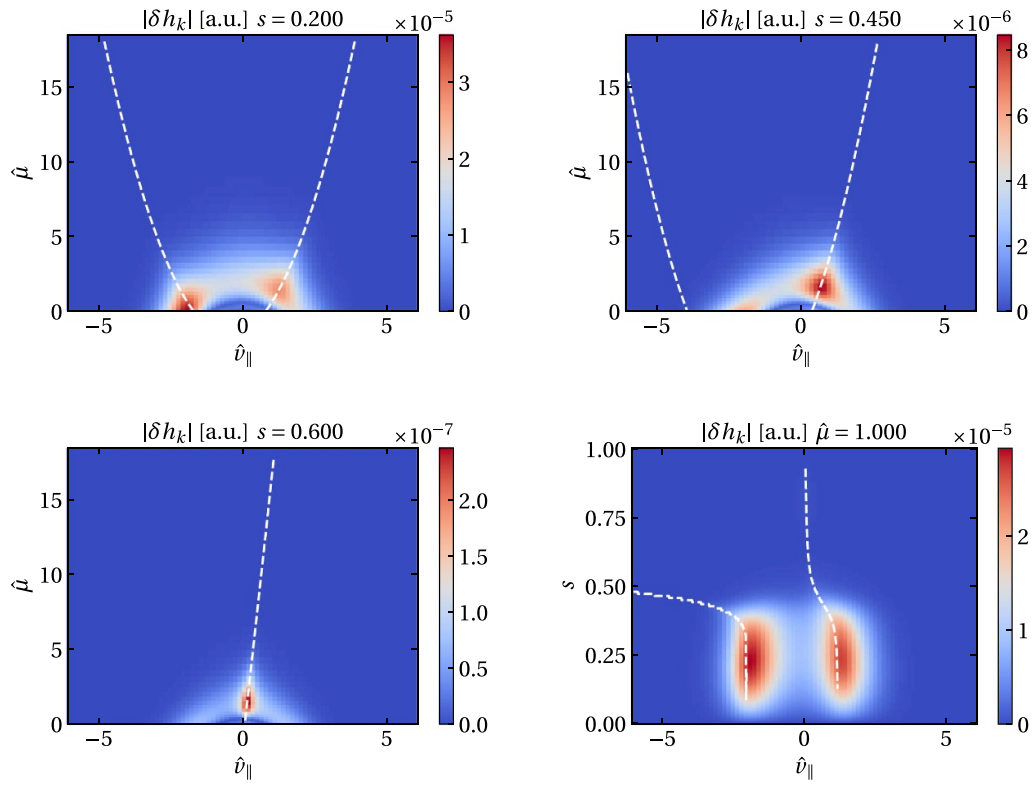


Figure 9. Same as figure 8 but for a case using a non-resonant safety factor profile and a standard monotonic pressure profile for the hot kinetic ions.

which is symmetric in $v_\parallel$. However, δh_k is strongly dominated by the $q < m/n$ region, as one can verify by comparing the maximum amplitude for the different radial locations. It can be seen that in the non-resonant case with non-monotonic hot pressure profile, there is no wave-particle resonance in the low shear region where the mode is developed. There is however such a resonance in the outer region, similarly to what is observed for the resonant case. The kinetic effect in the non-resonant case is however as big or even bigger than in the resonant case. As a consequence, one observes that presence or not of a $q = m/n$ resonance is not significant to predict the magnitude of kinetic effects. The same statement is also true for wave-particle resonances as discussed below.

The non-resonant case where the hot particles follow the standard pressure profile is shown in figure 9. A wave-particle resonance condition can be observed at most radial locations. The distribution function however aligns with the resonance only very loosely. One can note the presence in the inner region of two wave-particle resonant surfaces, one at negative and one at positive $v_\parallel$. A similar observation can be made in the resonant case (not shown here). It is interesting to see that these cases with standard hot pressure profile have a weak kinetic effect, despite the resonance that can be observed at almost all radial locations. A wave-particle resonance in the kinetic pressures is therefore not a sufficient condition to obtain a strong kinetic effect. On a more technical note, the advantages of the Case–Van Kampen formulation of the kinetic-MHD problem are evident here, since despite the presence of a resonant denominator in several cases in the solution of drift-kinetic equation, the `VENUS-KMHD` code is able to produce clean results without any difficulty.

The resonance condition used to draw the white dashed lines in figures 8 and 9 is:

$$-\Re(\omega) + \frac{F}{R_0 B}\frac{1}{qR_0}(m+nq)\,v_\parallel + \frac{F}{R_0 r q_k q B^4}\left(\frac{m_k v_\parallel^2 r F^2}{q^2 R_0^4} - \frac{\mu B}{2}\frac{\mathrm{d}\left(B^2\right)}{\mathrm{d}r}\right)\left(\left(\frac{r}{R_0}\right)^2 n - mq\right) = 0, \qquad (73)$$

which is simply the condition that should be satisfied for the denominator of equation (42) to cancel. Equation (73) describes a parabola. The $\frac{v_\parallel F}{qBR_0^2}(m+nq)$ term, often denoted as $k_\parallel v_\parallel$, is odd in $v_\parallel$ and cancels at the rational surface. It is responsible for the structure visible in figure 8 (*bottom right*), with a resonance located at positive $v_\parallel$ in the core region and at negative $v_\parallel$ beyond the rational surface. Since this

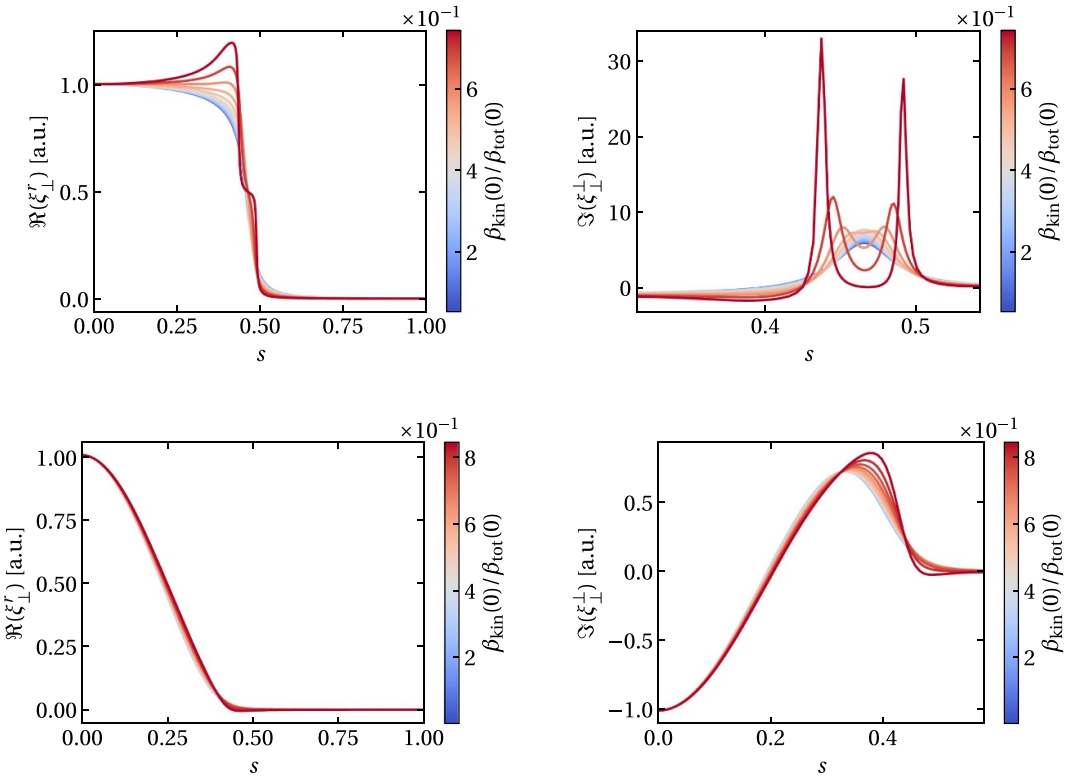


Figure 10. Radial (*left column*) and perpendicular (*right column*) components of the displacement for a resonant (*top row*) and a non-resonant (*bottom row*) safety factor profile for different hot particles pressures ($\beta_{\rm kin}(0)/\beta_{\rm tot}(0)$) in the case of a non-monotonic hot particles pressure. The perpendicular displacement $\xi_\perp^\perp$ is defined as the component of $\boldsymbol{\xi}_\perp$ that is perpendicular to both r and the equilibrium magnetic field $\boldsymbol{B}$. The colours indicate the kinetic fraction, that is the kinetic pressure divided by the total pressure on the magnetic axis.

term cancels at the rational surface and since all the other terms in (73) are even in $v_\parallel$, one also understands why a symmetric structure in $v_\parallel$ is observed at the rational surface.

As discussed above, one observes in figures 8 and 9 a resonant region of very different width, very narrow in the first case, very broad in the second. In order to find a possible explanation for this, one can write the resonant denominator of equation (42) as $\frac{1}{D(v_\parallel,\mu)-\omega}$, where using the same notation, equation (73) writes $D(v_\parallel,\mu)-\Re(\omega)=0$. One can then use the fact that $\left|\frac{1}{D(v_\parallel,\mu)-\omega}\right|^2 = \frac{1}{(D(v_\parallel,\mu)-\Re(\omega))^2+\gamma^2}$ to estimate the width in velocity space of the resonance region. It is characterised by the quantity $\Delta v = \frac{\gamma}{|\partial D/\partial v|}$. Note that the derivatives of D in $v_\parallel$ and μ involve quantities that are essentially the same in the two considered physical cases. The growth rate γ is however very different. One verifies in figure 7 (for $\beta_{\rm kin}(0)/\beta_{\rm tot}(0)=0.67$) that it is almost ten times larger in the case of figure 9 compared to the case of figure 8. This simple argument therefore explains why a very narrow resonant region is observed in velocity space in the latter case, while a much broader resonance is observed in the former case.

Finally, it is interesting to have a look at the mode structure with different values of the hot particles pressure. The radial structure of $\xi_\perp^r$ and $\xi_\perp^\perp$ is shown in figure 10 for a resonant and a non-resonant case using a non-monotonic hot particles pressure profile. In the non-resonant case, one observes that the mode structure is only very weakly affected by the kinetic effects. In the resonant case however, one observes a flattening of the mode around the ration surface, which is located here at $s=0.465$. This modification of the mode structure is more easily seen in the perpendicular displacement. When using the resonant $q-$profile, the peak formed by $\xi_\perp^\perp$ at the rational surface progressively splits in two on each side of the rational surface for increasing kinetic effects. This is consistent with the flattening observed in $\xi_\perp^r$ around the rational surface. The perpendicular displacement is proportional to the poloidal displacement $\xi_\perp^\theta$ which is itself approximately proportional to the radial derivative of $\xi_\perp^r$ (see the derivations in section 4.3). Further investigations would be required to understand the cause of this flattening. Finally,

it can be noticed that the mode with the strongest kinetic effects reach their maximum amplitude just before the rational surface instead of at the axis.

The observations in this section, while being specific to cylindrical geometry, are also relevant to the kinetic response associated with wave-circulating particle interaction in a torus. Nevertheless in a torus, toroidal curvature is important for circulating particles and critically important for the fraction of toroidally trapped particles, so significant new physics can be expected in future work in a torus.

6. Conclusion

A model for perpendicular kinetic-MHD in cylindrical geometry has been presented. We briefly introduced the new spectral kinetic-MHD code `VENUS-KMHD` based on the Case–Van Kampen approach. Although this code can solve kinetic-MHD cases in toroidal geometry, we focus here on the case of a cylinder (screw pinch geometry) to simplify the benchmarking process. The numerical methods used by `VENUS-KMHD` have nevertheless been briefly presented in the general toroidal case. Some key elements of the numerical implementation, such as the structure of the discretised matrices, convergence studies and the challenges associated with obtaining the physically most unstable mode were briefly mentioned but will be detailed further in a future work.

A number of exact semi-analytical and fully analytical results have been derived in cylindrical geometry to provide benchmarks for the newly implemented code. First, a benchmark of the non-adiabatic part of the distribution function has been presented in the general case. Expressions were derived for the kinetic perturbed pressures for known complex frequency and MHD displacement in $\mathcal{E}, \lambda$ velocity variables. The integral on the pitch angle has to be performed numerically. Good agreement was observed between the analytical expression and the `VENUS-KMHD` code for both the distribution function and the perturbed pressures. The section was completed by showing that using specific assumptions, it is possible to obtain fully analytical expressions for the kinetic perturbed pressures in $v_\parallel, \mu$ velocity variables. Once again, excellent agreement was observed.

Then, a benchmark of the full kinetic-MHD problem was demonstrated in two opposite limits, low and large frequency. In these limits, it is possible to obtain analytical solutions of the drift-kinetic equation, and therefore an exact expression of the kinetic effects can be obtained. We then used a vorticity operator to express one of the MHD displacement components in terms of the other and finally obtain a governing equation, which is an eigenvalue problem for the frequency of the mode and one component of the MHD displacement. The resulting governing equation was solved numerically and compared with the full kinetic-MHD code where the appropriate assumptions were applied in the considered limits. Good agreement was observed between the two approaches. In addition, it was shown for the first time that in the low-frequency limit, the kinetic effect cancels the energetic species contribution to the destabilising interchange term. Analogies were made with kinetic effects in a torus, which tend to cancel the destabilising effects of trapped ions in the fluid response. Some discrepancies were observed at larger total pressure, which is a known issue. We showed that in the large frequency limit, because of the weakness of the kinetic effects, it can be important to carefully include some higher order kinetic corrections in the computation, which in turn enables a match with the numerical results at higher β values.

Finally, it was shown that kinetic effects can drive instabilities in cylindrical geometry. The modes investigated were $m = n = 1$ fishbone-like instabilities, with resonance between the wave frequency and the guiding centre frequency of fast ions subject to curvature drift in the cylinder. While it is observed that kinetic effects are usually stabilising, cases of destabilisation were identified; for example when the hot pressure peaks outside the mode location and rapidly decreases towards the edge. Using such a hot pressure profile, we observe modes that would be ideally stable and that are driven unstable solely by kinetic effects. Most of the observed kinetic-MHD cases in a cylinder involve a resonant interaction between the guiding centre frequency (including the contribution from $v_\parallel \boldsymbol{b} \cdot \boldsymbol{\nabla} = k_\parallel v_\parallel$) of the particle and the mode frequency. These resonances would require very careful treatment if the kinetic response were to be solved instead using the standard Landau approach deployed in most other kinetic-MHD codes. Thanks to our code using the Case–Van Kampen approach, such resonant interactions can be solved in a straightforward way, without any specific caution. In this respect, we can therefore confidently expect success when solving for kinetic instabilities in a torus, especially because the adopted approach can handle arbitrary orbit width.

Acknowledgments

This work has been carried out within the framework of the EUROfusion Consortium, partially funded by the European Union via the Euratom Research and Training Programme (Grant Agreement No. 101052200 — EUROfusion). The Swiss contribution to this work has been funded in part by the Swiss State Secretariat for Education, Research and Innovation (SERI). Views and opinions expressed are however those of the author(s) only and do not necessarily reflect those of the European Union, the European Commission or SERI. Neither the European Union nor the European Commission nor SERI can be held responsible for them. This work was supported in part by the Swiss National Science Foundation.

Data availability statement

The data cannot be made publicly available upon publication because they are not available in a format that is sufficiently accessible or reusable by other researchers. The data that support the findings of this study are available upon reasonable request from the authors.

Author contributions

Fabien Jeanquartier 0009-0009-5683-2379
Data curation (equal), Formal analysis (equal), Investigation (equal), Software (equal), Visualization (equal), Writing – original draft (lead), Writing – review & editing (equal)

Jonathan P Graves 0000-0002-7959-7959
Conceptualization (equal), Funding acquisition (equal), Methodology (equal), Project administration (equal), Resources (equal), Supervision (equal), Writing – original draft (equal), Writing – review & editing (equal)

Stephan Brunner 0000-0001-7588-7476
Conceptualization (equal), Funding acquisition (equal), Methodology (equal), Project administration (equal), Resources (equal), Supervision (equal), Writing – original draft (equal), Writing – review & editing (equal)

Guillermo Bustos Ramirez 0009-0000-0509-0904
Methodology (equal), Software (equal), Writing – original draft (equal), Writing – review & editing (equal)

Tom Emerit 0009-0006-4206-7838
Data curation (equal), Formal analysis (equal), Investigation (equal), Validation (equal), Visualization (equal), Writing – original draft (equal), Writing – review & editing (equal)

Samuel Lanthaler 0000-0003-1911-246X
Methodology (equal), Software (equal), Writing – original draft (equal), Writing – review & editing (equal)

Amélie Renggli 0009-0001-0993-8092
Data curation (equal), Formal analysis (equal), Investigation (equal), Validation (equal), Visualization (equal), Writing – original draft (equal), Writing – review & editing (equal)

Appendix A

$X, \delta X$	Equilibrium and perturbed generic quantity,
[a.u.]	arbitrary units, typically because the amplitude of a linear mode is fixed arbitrarily,
μ_0	vacuum permeability,
Γ	adiabatic index,
$\boldsymbol{x}$	vector of unknowns, see equation (30),
r	radial variable,
s	normalised radial variable, see subsection 2.2, in a cylinder $s = r/a$,

θ	poloidal straight-field angle,
φ	toroidal angle,
(R, Z, φ)	cylindrical coordinate system,
R_0	major radius of tokamak equilibrium. In cylindrical geometry: $R_0 = L_z/2\pi$ with L_z the length of the cylinder,
a	minor radius of the tokamak or the cylinder equilibrium,
ϵ	inverse aspect-ratio,
$\mathcal{L}$	Lagrangian,
P_φ	canonical momentum conjugated to the toroidal angle,
$\mathcal{E}$	energy,
λ	pitch angle except in section 3: eigenvalue ($\lambda = -i\omega$),
v_{th_k}	thermal velocity of species k, $v_{\text{th}_k} = \sqrt{T_k(0)/m_k}$,
$v_\parallel$	parallel velocity,
$\hat{v}_\parallel$	normalised parallel velocity, $\hat{v}_\parallel = v_\parallel / v_{\text{th}_k}$,
$\boldsymbol{v}_\perp$	perpendicular velocity,
μ	magnetic moment,
$\hat{\mu}$	normalised magnetic moment, $\hat{\mu} = \mu B_{\text{ref}}/T_k(0)$,
$\boldsymbol{v}_{\boldsymbol{g_k}}$	guiding-centre velocity for species k, see equation (9),
$\boldsymbol{j}$	electric current,
$\boldsymbol{E}$	electric field,
$\boldsymbol{A}$	vector potential,
ϕ	electrostatic potential,
$\boldsymbol{B}$	magnetic field,
$\boldsymbol{b}$	unit vector parallel to the magnetic field ($\boldsymbol{B}/B$),
F	RB_φ, see equation (4),
$\boldsymbol{\kappa}$	magnetic curvature,
q	safety factor profile,
Δq	deviation from the rational surface, see equation (43),
q_s	safety factor at the rational surface, typically 1 in this work,
r_s	radial location of the rational surface, $q(r_s) = q_s$,
ψ	poloidal magnetic flux,
$\xi_\perp^r$, $\xi_\perp^\perp$	radial and perpendicular components of the perpendicular MHD displacement,
$\delta u_\perp^r$, $\delta u_\perp^\perp$	radial and perpendicular components of the perpendicular perturbed fluid velocity,
m	poloidal Fourier mode,
n	toroidal Fourier mode,
ω	(complex) mode frequency,
γ	growth rate $\gamma = \Im(\omega)$,
$\Delta\gamma_{\text{kin}}$	kinetic correction on the growth rate, see equation (64),
ω_R	real mode frequency, $\omega_R = \Re(\omega)$,
ω_d^φ	drift frequency, see equation (43),
ω_{d0}^φ	modified drift frequency, see equation (44),
ω_*	diamagnetic frequency, $\omega_* = -\left(\frac{q}{q_k}\frac{\partial F_k}{\partial \psi}\right) / \left(\frac{\partial F_k}{\partial \mathcal{E}}\right)$,
ω_{A}	Alfvén frequency, including the density of all species, evaluated at the magnetic axis,
V_r	radial vorticity operator, see equation (56),
V_φ	toroidal vorticity operator, see equation (57),
i	unit imaginary number, index of all the species (kinetic and non-kinetic),
j	index of the non-kinetic species,

k	index of the kinetic species,
P_i	pressure of species i,
P	total equilibrium pressure summed over all species,
P_{fluid}	equilibrium pressure of the non kinetic species, $P_{\text{fluid}} = \sum_j P_j$,
β_{tot}	normalised plasma pressure for all the species $\beta_{\text{tot}} = \sum_i \mu_0 P_i / B^2$, sometimes simply called β,
β_{kin}	normalised plasma (equilibrium) pressure of the kinetic species, $\beta_{\text{kin}} = \sum_k \mu_0 P_k / B^2$,
α	normalised pressure gradient,
α_{kin}	normalised gradient of the equilibrium pressure associated with the kinetic species,
$\delta P^{\text{tot}}_{\perp,\parallel_k}$	full perpendicular/parallel perturbed pressure for species k, computed as a moment of δf_k, includes adiabatic and kinetic effects, see equation (6),
$\delta P_{\perp,\parallel_k}$	kinetic perpendicular/parallel perturbed pressure for species k, computed as a moment of δh_k, includes adiabatic and kinetic effects, see equation (17),
f_k	total (nonlinear) distribution function for species k,
F_k	equilibrium (background) distribution function for species k,
δf_k	fluctuating part of the distribution function for species k,
$\delta f_{\text{adiab}_k}$	adiabatic part of the fluctuating distribution function for species k,
δh_k	non-adiabatic part of the fluctuating distribution function for species k,
n_i	number density profile of species i,
q_i	electric charge of species i,
m_i	mass of species i,
T_i	temperature profile of species i,
ρ_i	mass density for species i,
ρ	total mass density (summed over all species),
Δx	grid spacing for variable $x = r, m, v_\parallel, \mu$,
A	first matrix of the generalised eigenvalue problem,
B	second matrix of the generalised eigenvalue problem or norm of the magnetic field.

References

Antonsen T M and Bondeson A 1993 Effects of trapped thermal particles on the n = 1 internal kink mode in tokamaks *Phys. Rev. Lett.* **71** 2046–9

Antonsen T M and Lane B 1980 Kinetic equations for low frequency instabilities in inhomogeneous plasmas *Phys. Fluids* **23** 1205–14

Antonsen T M and Lee Y C 1982 Electrostatic modification of variational principles for anisotropic plasmas *Phys. Fluids* **25** 132–42

Balay S 2022 *Technical Report* ANL-21/39 - Revision 3.17 (Argonne National Laboratory)

Balay S, Gropp W D, McInnes L C and Smith B F 1997 Efficient management of parallelism in object oriented numerical software libraries *Modern Software Tools in Scientific Computing* ed E Arge, A M Bruaset and H P Langtangen (Birkhäuser Press) pp 163–202

Bratanov V 2011 Landau and van Kampen spectra in discrete kinetic plasma systems *PhD Thesis* LMU Munich

Bratanov V, Jenko F, Hatch D and Brunner S 2013 Aspects of linear Landau damping in discretized systems *Phys. Plasmas* **20** 022108

Briguglio S, Vlad G, Zonca F and Kar C 1995 Hybrid magnetohydrodynamic-gyrokinetic simulation of toroidal Alfvén modes *Phys. Plasmas* **2** 3711–23

Briguglio S, Zonca F and Vlad G 1998 Hybrid magnetohydrodynamic-particle simulation of linear and nonlinear evolution of Alfvén modes in tokamaks *Phys. Plasmas* **5** 3287–301

Bustos Ramirez G 2023 Exploration of the parameter space for the excitation and saturation of edge harmonic oscillations *PhD Thesis* EPFL (https://doi.org/10.5075/epfl-thesis-9763)

Case K 1959 Plasma oscillations *Ann. Phys.* **7** 349–64

Chavdarovski I and Zonca F 2014 Analytic studies of dispersive properties of shear Alfvén and acoustic wave spectra in tokamaks *Phys. Plasmas* **21** 052506

Chen L and Hasegawa A 1991 Kinetic theory of geomagnetic pulsations: 1. internal excitations by energetic particles *J. Geophys. Res. Space Phys.* **96** 1503–12

Cheng C Z 1991 A kinetic-magnetohydrodynamic model for low-frequency phenomena *J. Geophys. Res.* **96** 21159–71

Cheng C 1991 Alpha particle destabilization of the toroidicity-induced Alfvén eigenmodes *Phys. Fluids B* **3** 2463–71

Cheng C 1992 Kinetic extensions of magnetohydrodynamics for axisymmetric toroidal plasmas *Phys. Rep.* **211** 1–51

Dalcin L D, Paz R R, Kler P A and Cosimo A 2011 Parallel distributed computing using Python *Adv. Water Resour.* **34** 1124–39

Degtyarev L, Martynov A, Medvedev S, Troyon F, Villard L and Gruber R 1997 The KINX ideal MHD stability code for axisymmetric plasmas with separatrix *Comput. Phys. Commun.* **103** 10–27
Deng W, Lin Z and Holod I 2012 Gyrokinetic simulation model for kinetic magnetohydrodynamic processes in magnetized plasmas *Nucl. Fusion* **52** 023005
Fried B D and Conte S D 1961 *The Plasma Dispersion Function* (Academic) (https://doi.org/10.1016/C2013-0-12176-9)
Fu G Y, Park W, Strauss H R, Breslau J, Chen J, Jardin S and Sugiyama L E 2006 Global hybrid simulations of energetic particle effects on the n = 1 mode in tokamaks: internal kink and fishbone instability *Phys. Plasmas* **13** 052517
Graves J P 2020 Private notes
Graves J P, Chapman I, Coda S, Eriksson L G and Johnson T 2009 Sawtooth-control mechanism using toroidally propagating ion-cyclotron-resonance waves in tokamaks *Phys. Rev. Lett.* **102** 065005
Graves J P, Coste-Sarguet M and Wahlberg C 2021 Pressure driven long wavelength MHD instabilities in an axisymmetric toroidal resistive plasma *Plasma Phys. Control. Fusion* **64** 014001
Graves J P, Sauter O and Gorelenkov N N 2003 The internal kink mode in an anisotropic flowing plasma with application to modeling neutral beam injected sawtoothing discharges *Phys. Plasmas* **10** 1034–47
Graves J P and Wahlberg C 2017 Generalised zonal modes in stationary axisymmetric plasmas *Plasma Phys. Control. Fusion* **59** 054011
Graves J P, Zullino D, Brunetti D, Lanthaler S and Wahlberg C 2019 Reduced models for parallel magnetic field fluctuations and their impact on pressure gradient driven MHD instabilities in axisymmetric toroidal plasmas *Plasma Phys. Control. Fusion* **61** 104003
Graves J 2013 Toroidal drift precession and wave-particle interaction in shaped tokamaks with finite beta and neoclassical equilibrium effects *Plasma Phys. Control. Fusion* **55** 074009
Graves J, Hastie R and Hopcraft K 2000 The effects of sheared toroidal plasma rotation on the internal kink mode in the banana regime *Plasma Phys. Control. Fusion* **42** 1049
Gruber R and Rappaz M 2012 *Finite Element Methods in Linear Ideal Magnetohydrodynamics* (*Scientific Computation*) (Springer) (https://doi.org/10.1007/978-3-642-86708-8)
Hastie R and Hender T 1988 Toroidal internal kink stability in tokamaks with ultra flat q profiles *Nucl. Fusion* **28** 585
Hernandez V, Roman J E, Tomas A and Vidal V 2007 Krylov-Schur methods in SLEPc *Technical Report* STR-7 (Universitat Politècnica de València)
Hernandez V, Roman J and Vidal V 2005 SLEPc: a scalable and flexible toolkit for the solution of eigenvalue problems *ACM Trans. Math. Softw.* **31** 351–62
Hirshman S and Whitson J 1983 Steepest-descent moment method for three-dimensional magnetohydrodynamic equilibria *Phys. Fluids* **26** 3553–68
Jenko F, Dorland W, Kotschenreuther M and Rogers B N 2000 Electron temperature gradient driven turbulence *Phys. Plasmas* **7** 1904–10
Kerner W, Goedbloed J, Huysmans G, Poedts S and Schwarz E 1998 CASTOR: normal-mode analysis of resistive MHD plasmas *J. Comput. Phys.* **142** 271–303
Kruskal M D and Oberman C R 1958 On the stability of plasma in static equilibrium *Phys. Fluids* **1** 275–80
Lanthaler S 2020 Kinetic-MHD stability of virtually collisionless plasmas *PhD Thesis* EPFL (https://doi.org/10.5075/epfl-thesis-10142)
Lanthaler S, Graves J P, Pfefferlé D and Cooper W A 2019 Guiding-centre theory for kinetic-magnetohydrodynamic modes in strongly flowing plasmas *Plasma Phys. Control. Fusion* **61** 074006
Lanti E *et al* 2020 Orb5: a global electromagnetic gyrokinetic code using the pic approach in toroidal geometry *Comput. Phys. Commun.* **251** 107072
Lauber P, Günter S, Könies A and Pinches S 2007 LIGKA: a linear gyrokinetic code for the description of background kinetic and fast particle effects on the MHD stability in tokamaks *J. Comput. Phys.* **226** 447–65
Liu D, Liu Y, Heidbrink W, Van Zeeland M, Zhou L, Austin M and Marinoni A 2022 Effect of anisotropic fast ions on internal kink stability in DIII-D negative and positive triangularity plasmas *Nucl. Fusion* **62** 112009
Liu Y, Chu M S, Chapman I T and Hender T C 2008 Toroidal self-consistent modeling of drift kinetic effects on the resistive wall mode *Phys. Plasmas* **15** 112503
Liu Y, Chu M, Chapman I and Hender T 2009 Modelling resistive wall modes in ITER with self-consistent inclusion of drift kinetic resonances *Nucl. Fusion* **49** 035004
Lütjens H and Luciani J F 2010 XTOR-2F: a fully implicit Newton-Krylov solver applied to nonlinear 3D extended MHD in tokamaks *J. Comput. Phys.* **229** 8130–43
McMillan B 2023 Relationship between drift kinetics, gyrokinetics and magnetohydrodynamics in the long-wavelength limit *J. Plasma Phys.* **89** 905890115
Ng C S, Bhattacharjee A and Skiff F 1999 Kinetic eigenmodes and discrete spectrum of plasma oscillations in a weakly collisional plasma *Phys. Rev. Lett.* **83** 1974–7
Park W *et al* 1992 Three-dimensional hybrid gyrokinetic-magnetohydrodynamics simulation *Phys. Fluids B* **4** 2033–7
Porcelli F, Stankiewicz R, Kerner W and Berk H 1994 Solution of the drift-kinetic equation for global plasma modes and finite particle orbit widths *Phys. Plasmas* **1** 470–80
Romero E and Roman J E 2014 A parallel implementation of Davidson methods for large-scale eigenvalue problems in SLEPc *ACM Trans. Math. Softw.* **40** 13:1–13:29
Schaumans C and Graves J P 2025 Ideal magnetohydrodynamic instabilities in tokamaks driven by strong toroidal plasma rotation: an analytical and numerical investigation *Plasma Phys. Control. Fusion* **67** 065021
Solov'ev L 1968 The theory of hydromagnetic stability of toroidal plasma configurations *Sov. J. Exp. Theor. Phys.* **26** 400
Van Kampen N 1955 On the theory of stationary waves in plasmas *Physica* **21** 949–63
Vlad G *et al* 2025 State of the art of gyrokinetic and hybrid MHD-kinetic codes through non-linear benchmarking to study reactor relevant burning plasmas *Rev. Modern Plasma Phys.* **9** 27
Waelbroeck F L 1989 Nonlinear growth of the quasi-interchange instability *Phys. Fluids B* **1** 499–505
Wesson J A 1986 Sawtooth oscillations *Plasma Phys. Control. Fusion* **28** 243
Wolfram Research Inc. 2017 Mathematica, version 11.1
Zhang H X, Zhang H W, Ma Z W and Liu C 2024 Influences of δb contribution and parallel inertial term of energetic particles on MHD-kinetic hybrid simulations: a case study of the 1/1 internal kink mode *Plasma Phys. Control. Fusion* **67** 015033
Zonca F and Chen L 2006 Resonant and non-resonant particle dynamics in Alfvén mode excitations *Plasma Phys. Control. Fusion* **48** 537